8. ASSESSMENT OF LOW-ASPECT-RATIO TOKAMAK POWER PLANT

Charles G. Bathke
Michael Billone
Leslie Bromberg
David A. Ehst
Laila A. El-Guebaly
Stephen C. Jardin
Hesham Y. Khater
Charles E. Kessel, Jr.
Tak-Kuen Mau
Farrokh Najmabadi
Michael Sidorov
Don Steiner
Igor N. Sviatoslavsky
Dai-Kai Sze
Mark S. Tillack
Peter Titus
Clement P. C. Wong

Contents

8.1. INTRODUCTION 8-1

8.2. PHYSICS ASSESSMENT 8-2

8.2.1. Equilibrium and Vertical Stability 8-2

8.2.2. MHD stability and bootstrap current 8-5

8.2.3. Current drive 8-9

8.2.4. Summary 8-13

8.3. ASSESSMENT OF ENGINEERING ASPECTS 8-14

8.3.1. Introduction 8-14

8.3.2. Center-Post Assessment 8-16

8.3.3. Design Implications of Copper and Copper Alloy Embrittlement . 8-22

8.3.4. TF-Coil Power Supply and Busbar 8-30

8.3.5. Shielding Options, Radiation Effects, and Activation 8-35

8.3.6. Blanket and Power Conversion Assessment 8-46

8.3.7. Divertor Assessment 8-50

8.4. SYSTEMS ASSESSMENT 8-52

8.4.1. Low-Aspect-Ratio-Tokamak Systems Models 8-52

8.4.2. Sensitivity Studies 8-54

8.4.3. Design Point Determination 8-64

8.5. SUMMARY & CONCLUSIONS 8-67

REFERENCES 8-68

8. ASSESSMENT OF LOW-ASPECT-RATIO TOKAMAK POWER PLANT

8.1. INTRODUCTION

The low-aspect-ratio tokamak is one of several power plant candidates which were assessed within the Starlite project. For all of the assessments, the existing literature and databases were relied upon heavily. New analyses were performed only for those features which are unique to the low-aspect-ratio tokamak power plant, and which required additional work in order to properly address the requirements and issues.

A methodology was developed for evaluating all fusion power plant design options in a consistent manner [1]. This methodology is based on a set of minimum requirements that must be met in order that a fusion power plant will be judged sufficiently attractive such that it will be able to compete with alternative energy sources and penetrate the energy marketplace during the 21st century. The requirements relate to economic, safety and environmental features that present-day utility and government representatives believe will be necessary in the future.

Uncertainties in basic data and in component performance remain for all fusion power plant options. In some cases the uncertainties are modest and in other cases they are large enough to cast serious doubts on the feasibility of the concept. It is essential in any assessment of options to factor these "key issues" into the evaluation. It is usually true that attractiveness and feasibility trade off against one another; new ideas which appear more attractive than existing "worked-out" designs often carry with them significant uncertainties. Conversely, a larger data base always allows a better understanding of the limitations and problems with a concept.

In this section, we present our assessment of low-aspect-ratio tokamak power plants. This assessment includes the results of detailed physics calculations, preliminary engineering design considerations, and parametric systems analyses. Although our assessment of low-aspect-ratio tokamak power plants was not comprehensive, we believe that we have identified and evaluated the key issues associated with this concept. In this regard, our study will provide an excellent starting point of departure for further analysis and assessment of the low-aspect-ratio tokamaks.

8.2. PHYSICS ASSESSMENT

The distinguishing feature of the low-aspect-ratio tokamak is that the Toroidal Field (TF) coils are made of copper or copper alloy rather than of superconductor, and that there are no ohmic-heating (OH) poloidal-field (PF) coils on the inboard side of the torus. These two features allow a design with little or no shielding on the inboard side of the tokamak and with very low aspect ratio ($A = R/a$ where R and a are the major and minor radii of plasma, respectively). In tokamak with superconducting TF coils, the natural increase in β with decreasing aspect ratio, (*i.e.,* $\beta \sim A^{-1}$ at fixed β_N and q_*) is offset by the decrease in the toroidal field strength at the plasma center set by the maximum allowable field at the superconductor (*i.e.,* $B_T \sim A^{1/2}$ for fixed B_{max} at the superconductor and with shielding present). This trade-off may not be present in tokamaks with normal-conducting coils in which the inboard shielding requirements are greatly reduced from that in a superconducting tokamak. Thus, in the low-aspect-ratio tokamak there is a net gain in the fusion power density $\beta^2 B_T^4$ as A is decreased at fixed β_N and q_*. If we combine this effect with the observed tendency for β_N to increase as A decreases, and if we make use of a class of high-bootstrap fraction equilibria (with high central safety factor q_0) to minimize the current drive requirements, then we find a potentially attractive configuration at low A with an increased mass power density over conventional designs [2]. The main drawbacks appear to be the large recirculating power associated with the ohmic losses in the TF coils and, perhaps, with the current-drive systems, and the lack of a substantial experimental database. In this section we describe the detailed equilibrium, MHD stability, and current drive calculations that were done within the Starlite project in support of the low-A design.

Throughout this section, the toroidal β is defined as $\beta_T = 2\mu_o\langle p\rangle/B_T^2$, the circularized safety factor, $q_* = 2\pi a^2 B_T S/\mu_o R I_p$, the normalized β $\beta_N = 100 \times \beta_T/(I_P/aB_T)$, the ratio of TF coil currents to the plasma current $I_{TF}/I_P = A^2 q_*/S$, where the shape factor $S = (1+\kappa^2)/2$. Here, $\langle p\rangle$ denotes the volume averaged pressure, B_T is the toroidal field in vacuum at the plasma major radius R, and I_p is the total plasma current. Also, κ is the elongation, and δ is the triangularity, ℓ_i is the internal inductance, and β_p is the poloidal β of the plasma.

8.2.1. Equilibrium and Vertical Stability

It is well known that reducing the plasma aspect ratio leads to larger plasma elongation in a uniform vertical field [3–9]. In a truly uniform vertical field the decay index

would be zero, so that the plasma would not be vertically unstable even though it might have significant elongation. Thus, so long as the plasma takes on an elongation less than the value obtained in a uniform magnetic field, it would not need a vertical control system.

As the aspect ratio is reduced the plasma distorts its shape to maintain force balance. In fact, the entire plasma shape changes, not just its elongation, as has been the emphasis in previous studies. In order to assess the plasma shape changes as a function of aspect ratio, the Tokamak Simulation Code (TSC) [10] is used with a multi-polar field specification [11] that allows for a uniform vertical field to the accuracy of the computer precision (10^{-12} in this case), guaranteeing that all gradients in the vertical magnetic field are negligible. The influence of the current profile (ℓ_i), the pressure (β_p), and the aspect ratio on the resulting free-boundary plasma shape is examined.

As the aspect ratio is reduced both the plasma elongation and triangularity increase, at rates which depend on the current profile and pressure. For example, for a set of equilibria with $\ell_i = 0.5$ and $\beta_p = 0.5$, as the aspect ratio decreases through 2.0, 1.5, 1.25, and 1.15, the plasma elongation increases sequentially through 1.4, 1.6, 1.8, and 1.9, and the triangularity increases through 0.1, 0.2, 0.35, and 0.47, respectively. The strong increase in triangularity is particularly important, since it has a strong stabilizing effect on $n > 0$ ideal MHD modes. Another very strong dependence of the plasma shape occurs as the plasma current profile is changed. At the fixed aspect ratio of 1.25, the plasma elongation at zero pressure varies from 1.5 to 3.3 as ℓ_i is varied from 1.35 to 0.15. The triangularity shows a similar rapid increase at very low values of ℓ_i, although not as large as the elongation. Variations in the pressure have a weaker effect on the plasma shape, decreasing the elongation and increasing the triangularity, as the pressure is increased. Finally, the effects of the detailed profiles were briefly examined. Two equilibria both with $\ell_i = 0.26$ and $\beta_p = 0.50$ but different current profiles were examined which had elongations of 1.75 and 1.83, and triangularities of 0.37 and 0.34, respectively. These results show that details of the plasma profiles will affect the plasma shape and should give rise to a band of possible values rather than a line. A number of these equilibria are reported in Table 8.2-I.

Once the aspect ratio has been determined, the primary issue in designing the poloidal-field (PF) system is the difference between the desired plasma shape and the natural plasma shape. If it is desired to have a larger elongation than occurs in the uniform vertical field, then a quadrapole field must be provided and a vertical-position control system will be required. If a smaller elongation is desired, then a quadrapole field with opposite polarity is required. The variations of plasma elongation with ℓ_i probably pose

Table 8.2-I.
Natural Shapes for Low-Aspect-Ratio Tokamaks

$A = 1.15$			$A = 1.25$			$A = 1.50$			$A = 2.00$		
$\ell_i(3)$, $\beta_p(1)$	κ	δ	$\ell_i(3)$, $\beta_p(1)$	κ	δ	$\ell_i(3)$, $\beta_p(1)$	κ	δ	$\ell_i(3)$, $\beta_p(1)$	κ	δ
0.43,1.00	1.907	0.539	0.44,1.00	1.834	0.425	0.48,1.00	1.629	0.260	0.51,1.00	1.364	0.125
0.52,1.00	1.762	0.507	0.53,1.00	1.700	0.390	0.56,1.00	1.533	0.238	0.59,1.00	1.322	0.114
0.63,1.00	1.641	0.488	0.64,1.00	1.590	0.372	0.67,1.00	1.451	0.226	0.69,1.00	1.280	0.108
0.82,1.00	1.507	0.476	0.83,1.00	1.460	0.362	0.83,1.00	1.364	0.217	0.84,1.00	1.230	0.105
0.98,1.00	1.437	0.472	0.97,1.00	1.400	0.354	0.99,1.00	1.308	0.215	0.99,1.00	1.196	0.104
1.13,1.00	1.389	0.471	1.12,1.00	1.357	0.354	1.13,1.00	1.270	0.214	1.13,1.00	1.172	0.105
1.34,1.00	1.337	0.471	1.35,1.00	1.300	0.357	1.33,1.00	1.232	0.214	1.31,1.00	1.147	0.105
0.27,0.50	2.270	0.576	0.31,0.50	2.110	0.440	0.37,0.50	1.775	0.251	0.46,0.50	1.402	0.106
0.36,0.50	2.057	0.521	0.40,0.50	1.930	0.397	0.46,0.50	1.657	0.225	0.54,0.50	1.361	0.097
0.46,0.50	1.894	0.492	0.49,0.50	1.793	0.373	0.56,0.50	1.565	0.211	0.63,0.50	1.323	0.092
0.62,0.50	1.711	0.471	0.65,0.50	1.640	0.352	0.71,0.50	1.464	0.201	0.77,0.50	1.275	0.089
0.77,0.50	1.609	0.462	0.81,0.50	1.538	0.343	0.86,0.50	1.401	0.197	0.91,0.50	1.242	0.089
0.93,0.50	1.536	0.459	0.96,0.50	1.475	0.341	1.00,0.50	1.356	0.196	1.04,0.50	1.219	0.089
1.14,0.50	1.467	0.457	1.16,0.50	1.414	0.338	1.18,0.50	1.313	0.198	1.22.0.50	1.195	0.091
1.41,0.50	1.402	0.458	1.56,0.50	1.337	0.345	1.43,0.50	1.273	0.201	1.44,0.50	1.171	0.094
0.15,0.00	3.334	0.530	0.14,0.00	3.323	0.445	0.31,0.00	1.961	0.205	0.42,0.00	1.445	0.079
0.25,0.00	2.634	0.484	0.22,0.00	2.664	0.385	0.37,0.00	1.859	0.191	0.50,0.00	1.400	0.071
0.41,0.00	2.117	0.447	0.32,0.00	2.262	0.348	0.45,0.00	1.726	0.176	0.58,0.00	1.360	0.068
0.56,0.00	1.882	0.428	0.47,0.00	1.918	0.317	0.60,0.00	1.585	0.164	0.72,0.00	1.311	0.066
0.72,0.00	1.750	0.423	0.62,0.00	1.747	0.307	0.74,0.00	1.501	0.161	0.85,0.00	1.278	0.066
0.92,0.00	1.639	0.422	0.77,0.00	1.644	0.302	0.87,0.00	1.446	0.161	0.98,0.00	1.254	0.067
1.18,0.00	1.546	0.425	0.96,0.00	1.554	0.301	1.05,0.00	1.395	0.163	1.14,0.00	1.231	0.070
1.52,0.00	1.468	0.430	1.36,0.00	1.447	0.309	1.28,0.00	1.349	0.168	1.36,0.00	1.209	0.073

the most difficult problem, since at higher ℓ_i a vertically destabilizing quadrapole field would be necessary to give the plasma the same elongation as is achieved naturally at low ℓ_i. The triangularity is relatively flat for values of ℓ_i between 0.5 and 1.5. However, if a higher value of triangularity is desired then a hexapole field must be applied. The hexapole may itself destabilize the plasma position, thus necessitating the superposition of a stabilizing quadrapole field.

8.2.2. MHD stability and bootstrap current

Initial stability studies of low aspect ratio tokamaks performed in support of the Starlite project concentrated on conventional first-stability current profiles with central safety factors near or slightly above unity, $q_0 \approx 1$ [12]. A scan of different pressure profiles for configurations with aspect ratios $1.2 < A < 2.5$, with shaping parameters $\kappa = 1.6$, $\delta = 0.35$ and monotonic current profiles such that $q_*/q_0 = 1.5$ or 3.0, revealed that configurations with broad pressure profiles in the range $p(0)/\langle p\rangle \sim 1.6 - 2.0$ maximize the stable β_N, and that β limit due to ballooning modes is smaller than that due to kink modes. In aspect ratio scans with these same parameters in which the pressure peaking factor is held fixed at $p(0)/\langle p\rangle = 1.8$, we find that the critical β_N for both low-n (kink) and high-n (ballooning) modes increases with decreasing A, and that this effect is particularly pronounced for the $n = 1$ kink mode, both with and without a conducting wall.

These initial studies were next extended to configurations with $q_0 > 1.1$ in order to achieve higher ballooning β limits and increased bootstrap fraction [13] (*i.e.,* the ratio of the plasma current arising from the bootstrap effect to the total plasma current). As the computed bootstrap fraction [14] began to approach unity, it became necessary to develop special techniques for computing low-A equilibria to assure that the pressure driven currents never exceeded the equilibrium currents, either globally or locally. (Note that by "pressure driven current", we refer to the combination of bootstrap, diamagnetic, and Pfirsch-Schlüter currents that all combine to provide toroidal plasma current from the plasma pressure. We use $f_{\nabla p}$ to denote the fraction of the total toroidal plasma current that is provided by all the pressure driven currents.) These high-bootstrap-fraction equilibria were further divided into two categories, those that require edge current drive and those that do not, depending on whether or not external current drive must be supplied outside the minor radius where the bootstrap current peaks (see Figs. 8.2-1 and 8.2-2). The maximum stable β is largest for equilibria in the first category, but the recirculating power associated with current drive is minimized by equilibria in the second

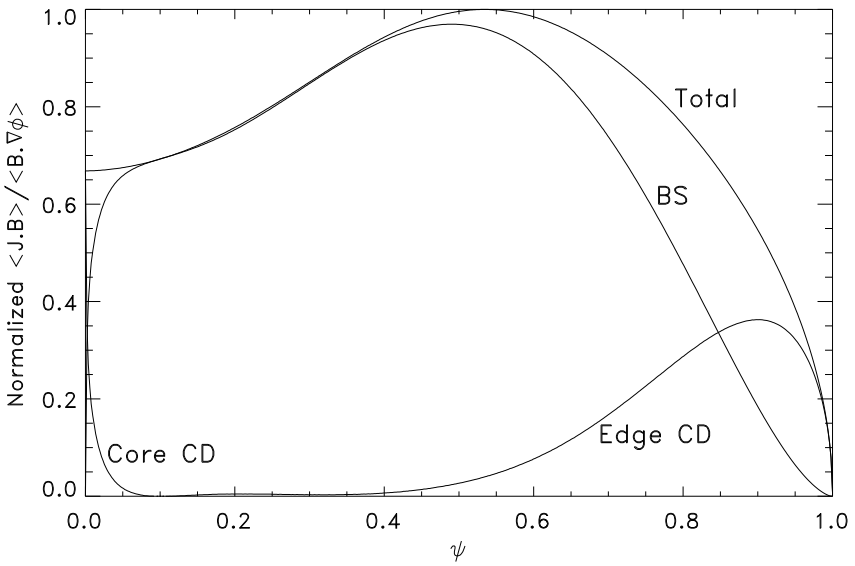

Figure 8.2-1. Parallel currents as functions of poloidal flux ψ for a high-bootstrap-fraction equilibrium which requires edge current drive.

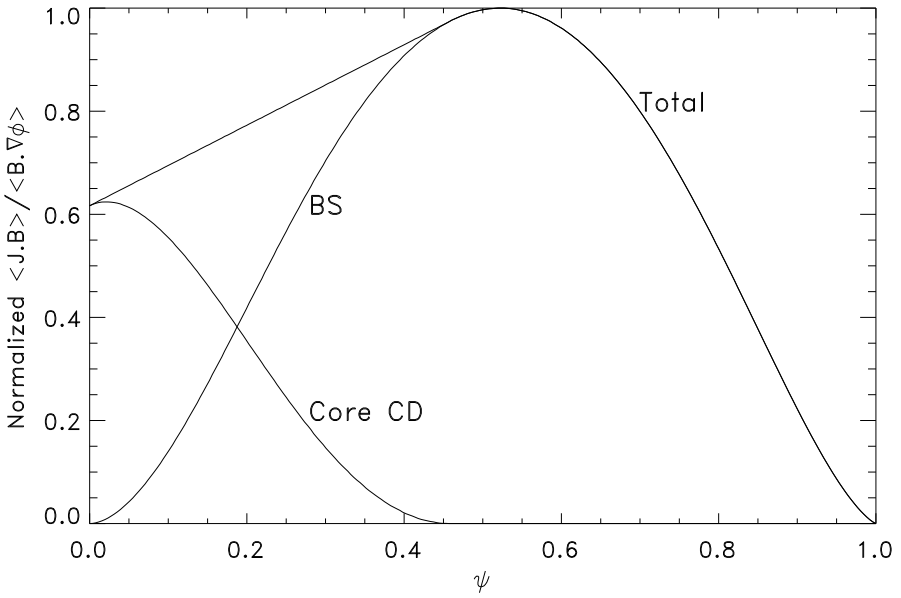

Figure 8.2-2. Parallel currents as functions of poloidal flux ψ for a high-bootstrap-fraction equilibrium which does not require edge current drive.

category (see Sec. 8.2.3). The high-bootstrap-fraction equilibria also tend to have very high edge q values, making it difficult for numerical stability codes to resolve the stability of intermediate-n modes. Some of the most interesting stable low-A equilibria found in these studies are listed in Table 8.2-II.

The first three equilibria in Table 8.2-II clearly illustrate the tradeoff between high pressure-driven current fraction (STREAC09 with $\beta_T = 12\%$, $f_{\nabla P} = 0.90$), high β (STREAC13 with $\beta_T = 80\%$, $f_{\nabla P} = 0.15$), and a reasonable compromise (STREAC06 with $\beta_T = 43\%$, $f_{\nabla P} = 0.85$). Cases requiring only central current drive in addition to the bootstrap current are marked "C", while those also requiring edge current drive are marked "C,E". STREAC06 and STREAC13 equilibria are stable to $n = 1, 2, 3$ with a conducting wall at $c/a \sim 1.24$ (where c is the distance of the wall from plasma center on mid-plane) and STREAC09 is stable to $n = 1$ with the same wall. The high edge q of STREAC09 makes the stability of $n = 2$ and higher mode number kinks exceedingly difficult to test. For the same reason, STREAC15 through STREAC19 equilibria have only been tested for ballooning stability but are presumed to be kink stable since these

Table 8.2-II.
Equilibrium Parameters for Stable Low-A Equilibria

CASE	A	κ	β_N	β_T	q_*	q_0	$f_{\nabla P}$	I_{TF}/I_P	Current-drive location
STREAC06	1.25	2.00	8.8	43%	2.38	3.3	0.85	1.27	center & edge
STREAC09	1.25	2.00	5.8	12%	5.83	3.3	0.90	3.12	center
STREAC13	1.25	2.00	4.6	80%	0.74	1.3	0.15	0.35	center & edge
STREAC15	1.25	2.20	6.5	17%	4.48	4.0	0.95	2.39	center
STREAC16	1.25	2.20	6.5	21%	3.63	4.0	0.85	1.95	center
STREAC17	1.40	2.20	7.0	16%	4.52	3.9	0.97	3.03	center
STREAC18	1.40	2.20	7.0	21%	3.45	4.0	0.89	2.32	center
STREAC19	1.25	3.00	7.0	40%	3.51	3.0	0.99	1.09	center

cases are similar to STREAC09. Without the wall for stabilization, the best case found at aspect ratio 1.25 has $\beta_T = 27\%$ and $f_{\nabla P} = 0.41$.

Since the power requirements associated with the edge current drive turned out to be so large (Sec. 8.2.3), our final studies concentrated on a series of equilibria that require only central current drive. We impose the constraint that the surface averaged parallel current density $\langle \mathbf{J} \cdot \mathbf{B} \rangle / \langle \mathbf{B} \cdot \nabla \phi \rangle$ be a linear function of the poloidal flux ψ interior to the point where the linear profile is tangent to the bootstrap current profile and equal to the bootstrap current outside this point (Figure 8.2-2). This constraint completely specifies the profiles and insures that the first derivatives of equilibrium quantities are continuous everywhere.

For these scans, we kept the shape fixed with $\kappa = 2.2$ and $\delta = 0.45$, but looked at two aspect ratios, $A = 1.25$ and $A = 1.4$. For each configuration we considered four different pressure profiles with a range of peaking factors, and for each pressure profile three density profiles were considered for a total of 12 different profile combinations. The density and pressure profiles were functions of the form $f \sim (1 - \hat{\psi}^{\beta})^{\alpha}$, where $\hat{\psi}$ is the normalized poloidal flux. For the initial $A = 1.25$ scan for instance, the pressure profiles we considered had the following exponents: $\alpha = 2$ and $\beta = 4$, 2.5, 1.5, and 1.0. For each pressure profile, three normalized density profiles used which were equal to the normalized pressure profile raised to the 3/4, 1/2, and 1/4 power. For each of these, we determined the maximum ballooning-stable β as a function of the central safety factor, q_0. After determining the optimum q_0 and pressure and density profiles, we refined the profiles with q_0 fixed to further optimize β. The STREAC15 through STREAC18 equilibria in Table 8.2-II contain some of the most attractive low-A equilibria found in this scan.

Finally, we performed a series of runs at aspect ratio $A = 1.25$ and with plasma elongations considerably above the natural elongation of about 2.2. These runs were specifically aimed at finding stable profiles that had near 100% self-driven current and high β at the higher elongations. In these runs, we employed the built-in constraint of no edge current drive. The best configuration found in this extensive scan is STREAC19. This equilibrium has an elongation of 3.0, which will certainly necessitate a vertical position control system. However, over 99% of the plasma current is self-driven for this configuration, and the β is 40%. Because of these two features, STREAC19 has been chosen as our baseline for assessment of low-A tokamak power plants. (Note that in the systems-code analysis, and in the engineering design, the β is reduced to 36%, consistent with the Starlite guideline of operating the power-plant plasma at 90% of the theoretical stability β limit)

8.2.3. Current drive

In the Low-A tokamak concept, externally generated RF waves must be used to sustain the necessary seed current; *i.e.,* the difference between the plasma current needed for equilibrium and stability and that provided by the bootstrap and other pressure-driven effects. The high plasma dielectric constant, approximately equal to the squared ratio of the electron plasma frequency to the electron cyclotron frequency in these configurations , f_{pe}^2/f_{ce}^2, precludes the use of either electron-cyclotron or lower-hybrid waves from penetrating into the core of the plasma. However, we find that the superposition of three conventional RF current drive techniques can provide the required seed current profile. These are (1) low-frequency fast waves (LFFW) with $f < f_{cT}$ for central region ($\hat{\psi} < 0.4$), (2) high-frequency fast waves (HFFW) with $f \sim 20 f_{cD}$ for mid-plasma region ($0.4 \leq \hat{\psi} \leq 0.8$), and (3) lower hybrid (LH) waves for edge-plasma region ($0.8 < \hat{\psi} < 1.0$). We attempt to obtain the best possible match between the RF-driven and seed current profiles by selecting the power spectra launched by the antenna and the launcher poloidal location on the outboard edge.

The CURRAY ray tracing code was used for the analysis [15]. This code utilizes the full Hirshman-Sigmar bootstrap current model [14] and includes three distinguishing features applicable to a low-A tokamak power plant: (a) high-β effects on HFFW dispersion and damping, (b) slowing-down α-particle absorption in the unmagnetized approximation, and (c) perpendicular thermal ion Landau damping for HFFW and LH waves. The local current-drive efficiencies include the deleterious effect of trapped electrons, which can be substantial in the outer part of the plasma.

Extensive current-drive calculations on four of the low-A equilibria listed in Table 8.2-II, namely, STREAC06, STREAC15, STREAC16, and STREAC17, reveals a large amount of power is needed to drive currents in the mid-plasma region ($0.4 < \hat{\psi} \leq 1$). This is exemplified by STREAC06 equilibria given in Table 8.2-II. The following parameters were used for current-drive calculations: $R = 3.0$ m, $a = 2.4$ m, $B_T = 2.37$ T, $I_p = 27.9$ MA $q_0 = 3.36$, $\beta = 0.426$, $\beta_p = 1.23$, $p_0 = 1.479$ MPa, $n_0/\rangle n\langle = 1.32$, and $T_0/\rangle T\langle = 1.32$. We also assumed that $n_e/n_i = 1.2$, $T_i/T_e = 0.9$, ion concentrations of $f_D = f_T = 0.43$ $f_{He} = 0.13$, and $f_{Oxygen} = 0.01$. The LFFW used for on-axis drive had a frequency of $f = 6$ MHz, the HFFW used for off-axis current drive had a frequency of $f = 236$ MHz, and the LH waves used for the edge drive had a frequency of $f = 1.1$ GHz. A temperature scan for the required current drive power in the three RF techniques used is presented in Table 8.2-III. As an example, Fig. 8.2-3 shows the profiles of the driven seed current calculated by the CURRAY code for the $\langle T_e \rangle = 15$ keV case of Table 8.2-III.

Table 8.2-III.
Temperature Scan of Current-Drive Power
for STREAC06 Low-A Equilibria

				Current-drive power (MW)			
$\langle T_e \rangle$ (keV)	$\langle n_e \rangle$ (m^{-3})	β_f/β	I_{BS}/I_P	P_{FW}	P_{HF}	P_{LH}	P_{tot}
8.0	3.69×10^{20}	0.02	0.769	76.6	807.5	131.7	1,015.8
12.0	2.37×10^{20}	0.06	0.786	21.4	542.0	153.6	617.0
15.2	1.82×10^{20}	0.09	0.785	15.1	324.8	130.2	370.1
20.0	1.32×10^{20}	0.13	0.789	13.2	262.6	17.0	292.8

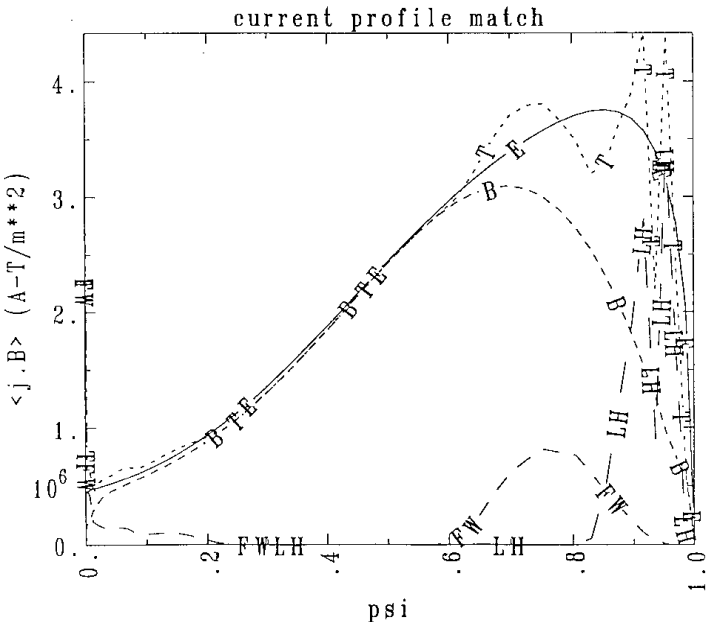

Figure 8.2-3. Current density profiles calculated from the CURRAY code for the $\langle T_e \rangle = 15$ keV case of Table 8.2-III. Curves labeled E, B, FW, LH and T correspond to equilibrium, bootstrap, fast-wave, lower-hybrid, and total driven current densities, respectively.

It is clear from examination of the table that the power requirements are dominated by the high-frequency fast-wave component. The reason for the high current-drive power required (or low current-drive efficiency) in that region of the plasma is twofold: (1) the current carrying electrons are essentially thermal resulting in severe reduction of the local current-drive efficiency due to trapped electron effects, and (2) there is significant absorption of the wave power by the energetic α-particles and thermal fuel ions.

One obvious way to avoid the excessive power required for bulk current drive is to make use of equilibria that have current profiles that are well aligned with the bootstrap current profile in the outer part of the plasma, thus requiring only current drive on axis, even though they may have somewhat less attractive plasma β values. We have examined such a case in detail (STREAC15 equilibrium of Table 8.2-II). The parameters used for current-drive analysis were: $R = 3.0$ m, $a = 2.4$ m, $B_T = 2.73$ T, $I_p = 23.1$ MA, $q_0 = 4.0$, $\beta = 0.168$, $\beta_p = 1.72$, $p_0 = 1.668$ MPa, $n_0/\langle n\rangle = 1.48$, and $T_0/\langle T\rangle = 1.48$. All other parameters are the same as in current-drive analysis of STREAC06 which are reported in Table 8.2-III (*i.e.,* $n_e/n_i = 1.2$, $T_i/T_e = 0.9$, ion concentrations of $f_D = f_T = 0.43$ $f_{He} = 0.13$, and $f_{Oxygen} = 0.01$). Since only on-axis current drive is required, only the LFFW system is required to drive the seed current. The frequency used in this case is 10 MHz. A temperature scan of the required current drive power is given in Table 8.2-IV. As an illustration, the matching of the RF-driven and equilibrium current density profiles for the $\langle T_e\rangle = 20$ keV case for STREAC15 is displayed in Fig. 8.2-4. As shown in Table 8.2-IV, only 32.2 MW of current drive power is required in this particular example, about one tenth of what is typically required in STREAC06.

The STREAC19 equilibrium (Table 8.2-II) appears to be most attractive as a power-plant candidate equilibrium because it has a high β ($\beta = 40\%$), and a low field-utilization factor ($T_{TF}/I_P = 1.09$). In this equilibrium, the bootstrap current is almost perfectly aligned with the equilibrium current, requiring only 0.15 MA of seed current to be driven on axis. The plasma parameters were: $R = 3.0$ m, $a = 2.4$ m, $B_T = 2.59$ T, $I_p = 35.4$ MA, $q_0 = 2.97$, $\beta = 0.401$, $\beta_p = 1.41$, $p_0 = 1.818$ MPa, $n_0/\langle n\rangle = 1.62$, and $T_0/\langle T\rangle = 1.14$. All other parameters are the same as in current-drive analysis of STREAC06 which are reported in Table 8.2-III (*i.e.,* $n_e/n_i = 1.2$, $T_i/T_e = 0.9$, ion concentrations of $f_D = f_T = 0.43$ $f_{He} = 0.13$, and $f_{Oxygen} = 0.01$). A LFFW system at 8 MHz is used to drive the on-axis seed current. A temperature scan of the required current-drive power is given in Table 8.2-V. The current-drive power requirement for this case is in the range of 10 MW or less. We point out that the current-drive power will be extremely sensitive to slight mismatches in the current density profiles due to variations in the plasma density and pressure profiles and this issue should be addresses in future studies.

Table 8.2-IV.
Temperature Scan of Current-Drive Power
for STREAC15 Low-A Equilibria

$\langle T_e \rangle$ (keV)	$\langle n_e \rangle$ (m^{-3})	β_f/β	I_{BS}/I_P	P_{tot} (MW)
8.0	3.34×10^{20}	0.02	0.895	135.8
12.0	2.10×10^{20}	0.06	0.898	76.1
16.0	1.53×10^{20}	0.10	0.905	43.9
20.0	1.18×10^{20}	0.13	0.903	32.2

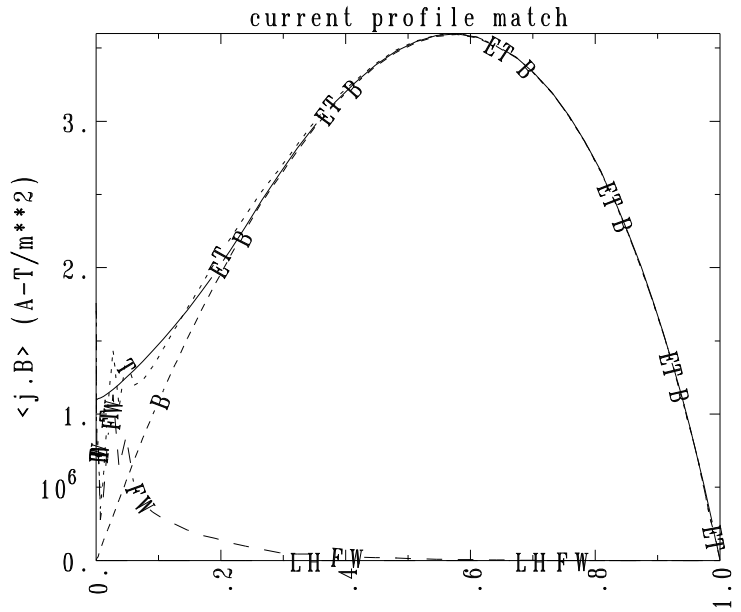

Figure 8.2-4. Current density profiles calculated from the CURRAY code for the $\langle T_e \rangle = 20$ keV case of Table 8.2-IV. Curves labeled E, B, FW, and T correspond to equilibrium, bootstrap, fast-wave, and total driven current densities, respectively.

Table 8.2-V.
Temperature Scan of Current-Drive Power
for STREAC19 Low-A Equilibria

$\langle T_e \rangle$ (keV)	$\langle n_e \rangle$ (m^{-3})	β_f/β	P_{tot} (MW)
12.0	3.20×10^{20}	0.045	10.5
14.0	2.70×10^{20}	0.050	8.3
16.0	2.33×10^{20}	0.065	6.2
18.0	2.03×10^{20}	0.080	5.1
20.0	1.82×10^{20}	0.090	4.4

8.2.4. Summary

The low-A tokamak may offer an alternative to the more conventional tokamak with an aspect ratio in the range of three to five. It has been shown that the natural elongation of a low-A tokamak increases with decreasing A and with decreasing ℓ_i and β_p. It has also been illustrated that there is a tradeoff between high pressure-driven current fraction and high β. However, configurations with elongations higher than the natural one offer the possibility of very low current-drive requirements simultaneous with moderately high β.

Equilibria that are stable to all MHD modes (with a conducting wall present) and that require very little current-drive power were found at $A = 1.25$, $\kappa = 3.0$, with $\beta = 40\%$. These would definitely require a vertical feedback system. All the cases shown here also require a conducting wall to stabilize the external kink mode, and thus future work must consider maintaining stability to the resistive wall mode [16]. In the absence of wall stabilization, the fraction of pressure driven current to total current would drop considerably. The sensitivity of current-drive power requirement to variations in the plasma profiles is an important issue that needs to be addressed, particularly for equilibria where the pressure-driven current fraction approaches unity.

8.3. ASSESSMENT OF ENGINEERING ASPECTS

8.3.1. Introduction

This section summarizes the engineering analyses and conclusions reached in support of the assessment of a fusion power plant based on a low-aspect-ratio tokamak. Engineering analyses were performed for two distinct purposes:

1. Direct analysis of the in-vessel components and engineering characteristics of the power plant allows us to evaluate its ability to meet some of its mission requirements, independent of the overall system performance. In addition, characterization of the key engineering issues in some cases requires more detailed analysis of individual components and systems.

2. Many of the attributes which affect the attractiveness of a power plant are computed in a self-consistent manner by the ARIES System Code [17]. Inputs to the code require decisions on the design of various components and a basic level of engineering analysis.

The assessment concentrated on the key components, including the center-post, first-wall and blanket, shielding, and divertor. To the extent possible, design concepts available from the existing literature were used for the assessments. In many cases, lack of detail or need for improvement was identified, suggesting that further design studies will be required in order to improve upon the assessments and to find innovative solutions to the problem areas which have been identified. Our physics understanding of the low-aspect-ratio tokamak is at an early stage of development; much of the engineering assessment is based on and sensitive to the reference set of physics parameters that were selected.

The center-post dominates the assessment. Minimizing the inboard radial build is well-known to be important for the overall success of the concept. However, an unshielded copper toroidal-field (TF) coil has many critical issues, which have been assessed. Activation analysis of the center-post indicates that the NRC Class-C waste-disposal limit can not be met unless the change-out time is extremely short (of the order of weeks). The volume of the waste stream would be quite large (the center-post alone weighs 680 tonnes, occupying 90 m^3). Given that the copper will embrittle quite rapidly under irradiation (some estimates are as low as 0.1 dpa), a mechanical design which is "licensable" must be developed. Code rules for brittle structures are unavailable, but it is likely that, at

a minimum, some additional measures will be needed to isolate the water coolant and provide some mechanical stability to prevent failure.

Mechanical analysis indicates that the compressive electromagnetic forces in the center-post are acceptable, but the tensile forces caused by the expansion of the TF-coils (appearing as vertical forces in the center-post) cannot be reacted by the copper center-post. For this reason a sliding connection between the upper end of the center-post and the outer leg of the TF-coils is proposed using mercury as the conducting material. Alternatively, electrical leads to the center-post can be located at this joint. The expansive forces from the TF-coils have to be reacted either by structure included in the shield around the copper center-post or by external structure.

Our analyses indicate that it is desirable to add 30 cm of shielding to the center-post. This level of shielding would help tremendously to reduce the waste-disposal problem, and reduce the change-out frequency. The volumetric heating of the shield ($\sim$150 MW) could be converted into electricity instead of being dumped at low temperature. A separate first wall could remove the surface heat load, protect against plasma erosion, add another level of safety assurance against center-post failure. This shield can also be used to mechanically stabilize the center-post. Depending on the final physics design point, it is probably more cost-effective to add a minimal and optimized shield rather than suffer the many penalties which arise from its absence.

Recirculating power could be a fatal flaw for the low aspect ratio tokamak. The primary sinks of power are the current-drive and TF-coil systems Estimates of the TF-coil losses for the cases examined here are extremely large. The reference design is a single-turn concept, as described in [18]. A single-turn TF coil avoids problems with insulator breakdown in the radiation environment and simplifies maintenance (although maintenance of the center-post remains a critical issue). The singe-turn coil, however requires large low-voltage, high-current power supplies and large bus-bars and leads. The ohmic losses are determined primarily from the basic system parameters. Given the high currents required, ways to reduce significantly these loads are to minimize the length, maximize the area (by pushing the post radius to the largest possible value), maintain low temperature (the conductivity of copper is sensitive to temperature), and minimize the neutron exposure. Scoping study of operation below room temperature to reduce the resistive losses suggests that cryogenic will not resolve the problem.

Besides concerns over the feasibility and consequences of the center-post, there are several unique constraints on the design of the blanket and divertor. These constraints arise due to the potentially high local power density, including peaking factors, and the

additional compatibility concerns with a water-cooled copper center-post. The divertor problem is especially severe, because the area available at low major radius is so restricted, and because additional sources of plasma heating (from current drive) add to the divertor heat loads. Even with significant flux expansion, the local surface heat flux is likely to exceed 10 MW/m^2.

The use of water in the center-post will make the use of liquid lithium in the power plant difficult or impossible. Additional barriers to leakage are necessary, and substantial additional analyses must be performed to satisfy licensing and regulatory requirements. The impact of ruling out liquid lithium is to reduce the bulk heat removal capabilities. In addition, no other coolant is known to be compatible with vanadium (compatibility with helium containing low levels of impurities is still uncertain), such that the design may be forced to use ferritic steel as the primary structural material and copper as a heat sink. These material choices further limit our ability to extract heat at high efficiency for the purpose of generating electricity, and further degrade the safety and environmental attractiveness of the concept.

8.3.2. Center-Post Assessment

8.3.2.1. Joule losses

The center-post of the low-aspect-ratio tokamak plays a major role in the design as well as the economics and safety of the machine. The reference design considered here utilizes a single-turn center-post; the back legs of all 16 TF coils connect to the center-post at the top and bottom. Thus, the center-post is the conduit for the return electrical current for all the TF coils. It is made of either pure copper or, more likely, dispersion-strengthened copper and cooled by water in the temperature range of 40 to 110 °C. Because the electrical current in the center-post is large and the cross section is small, the ohmic heating is high, despite the relatively low resistivity of copper.

The resistivity of metals increases with temperature, making it necessary to operate the center-post at a low temperature. As a result, the ohmic and nuclear heating cannot be converted to electricity. If the outlet temperature of the water is increased such that it could be used in a power cycle at a low conversion efficiency, the copper resistivity increases, resulting in drastic increase in Joule losses in the center-post such the net power consumed by the TF coils (Joule losses minus the recovered electricity) is increased. Further increase in resistivity due to transmutations compounds the problem.

Generally, a completely unshielded center-post has been proposed in fusion power plant studies based on low-aspect ratio tokamaks (*e.g.,* [18]). Rather high nuclear heating inside the copper center-post as well as high radiation damage and, therefore, a short lifetime result. Short lifetime has a large impact on the availability and waste disposal problems. For these reasons, a second design option has been investigated, employing a 30-cm thick shield around the copper center-post. The thermal analysis has been restricted to the ohmic heat input because this is by far the largest part of the total heat input and the nuclear heat is substantially different for the two design options. Nuclear heating requires either increased flow rate of the cooling water or an increase in the coolant temperature rise.

For the system code runs, the center-post average temperature was assumed to be 65 °C, and the resistivity of pure unirradiated copper was used. These are highly optimistic assumptions for several reasons (see Fig. 8.3-1):

Coolant temperature. Previous design studies have used a water inlet temperature of ∼40 °C and an outlet temperature over 100 °C. The copper temperature will exceed this value depending on the internal design and heat transfer coefficient (resistivity can easily be 25% higher).

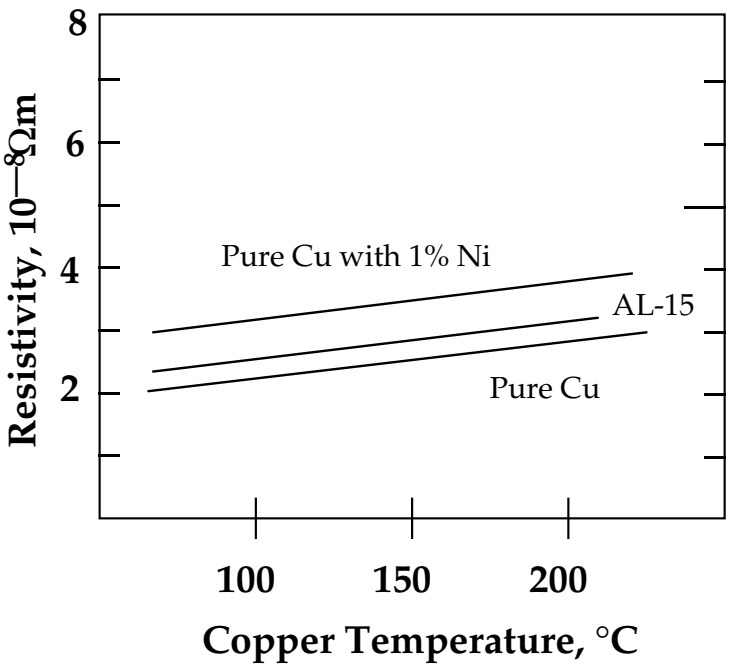

Figure 8.3-1. Resistivity of pure , dispersion-strengthened , and irradiated copper.

Copper alloying. Pure copper is weak at room temperature, and extremely weak at elevated temperatures. It is most likely that a dispersion-strengthened copper alloy would be needed in order to withstand the internal stresses generated by the high current. The resistivity of dispersion-strengthened copper (*e.g.,* GlidCop Al-15) is typically about 10% higher than pure copper.

Radiation damage. Nickel production is unavoidable in any copper alloy. Without inboard shielding, the nickel concentration will continue to build up. Depending on the lifetime of the center-post, the effect could be very significant. For example, analysis in Sec. 8.3.5 indicates that an average of ∼0.3% Ni impurity would exist after one full power year (FPY) of operation, contributing perhaps 20% to 30% additional ohmic losses. The peak damage is significantly higher, and can increase the resistivity by a factor of 2. Since the current density also is peaked at the location of peak damage, the net increase in ohmic losses will be compounded. Therefore, the center-post may have to be replaced even before its irradiation lifetime (or waste-disposal lifetime) is reached in order to limit this increase in the recirculating power.

8.3.2.2. Mechanical design of the center-post

The center-post is a relatively long, skinny column with a large aspect ratio. In addition to issues associated with its stability as a standing column, the center-post is subjected to compressive forces due to the current it carries, as well as tensile forces due to the loads applied by the outboard TF coil connections at the extremities of the center-post. Because copper becomes rapidly embrittled under a very low neutron fluence, the center-post is designed to carry only the radial compressive forces. This can be accomplished by providing a sliding electrical connection at the upper extremity, such that the expansive forces from the outboard TF coil legs are not transmitted to the center-post. Instead, these forces are reacted either by structure going through the inboard shield, all the way from the upper to the lower extremities or by external structure. In this way the expansive forces are reacted without impacting the center-post.

The pressure applied perpendicular to the direction of current is proportional to $B^2/2\mu_0$, where B is the magnetic field and μ_0 is the permeability of air (or vacuum). The magnetic field at the edge of the center-post conductor is ∼16 T, therefore, the pressure on the center-post is ∼100 MPa. This is larger than the yield strength of pure copper, indicating that probably the higher strength of dispersion-strengthened copper is needed. Table 8.3-I shows the yield strength of GlidCop C15720 irradiated to 15 dpa as 343 MPa or a factor of 2–3 higher than the magnetic pressure [19].

Table 8.3-I.
Tensile Properties Of Irradiated GlidCop Alloys [19]

		Tensile strength		Yield Strength			Reduction
Material	Condition	(MPa)	(KSI)	(MPa)	(KSI)	Elongation	in Area
C15720	Control	395	57	337	49	14%	48%
	3 dpa	411	60	353	51	14%	51%
	15 dpa	395	57	343	50	20%	50%
C15760	Control	466	68	397	58	12%	56%
	3 dpa	468	68	397	58	10%	43%
	15 dpa	449	65	379	55	11%	50%

The expansive force between the outboard TF horizontal legs can be found by taking moments about the point where the horizontal leg of the TF coil meets the vertical center-post. This moment, M, is given by

$$M = \int^{r_o} r_{cp}\, f(r)\, (r_o - r)\, dr\,, \tag{8.3-1}$$

where r_{cp} is the radius of the center-post, and r_o is the radius of the outboard return current. After integrating, the moment becomes:

$$M = 10^{-7} I^2 \left[r_o \ln\left(\frac{r_o}{r_{cp}}\right) + r_{cp} - r_o \right]\,, \tag{8.3-2}$$

where I is the total current. For $I = 40$ MA, $r_{cp} = 0.56$ m and $r_o = 17$ m, we calculate $M = 6.7 \times 10^9$ Nm. The tensile force is then M/r_o and the average tensile stress on the center-post is $M/(\pi r_{cp}^2 r_o)$. In this case the stress is at 415 MPa.

Noting that the tensile stresses would be much larger at the connection point between the outboard leg and the center-post, a sliding electrical connection is provided between the outboard TF coil leg and the center-post. The expansive force of 4×10^8 N would have to be reacted through structure placed either within the inner shield or externally.

Sliding electrical connection. A sliding electrical connection would only have to be provided on one end of the center-post with a rigid connection on the other end. At this point only one connection has been considered. This joint may be a natural location to attach the current leads to the TF coils. If the leads are located elsewhere, a conducting liquid such as mercury can be used to bridge the gap between the conducting members. In this case, we assume that a 0.5 cm gap exists between each TF coil leg and the center-post. Rolling bearings keep the TF coil legs concentric with the center-post, and the gap is filled with mercury. Mercury has a resistivity of 1.03 $\mu\Omega$-m at 100 °C and the contact area per TF coil is 1.1 m $\times$ 0.66 m. The electrical resistance of the gap is 7×10^{-9} Ω ohms and the ohmic heating per coil is 50 kW. The total ohmic dissipation for the 16 coils is 0.8 MW. Several issues have to be considered. Mercury forms amalgams with many metals. It may be necessary to electroplate the contacting parts with a metal with which it does not react with mercury. The mercury would have to be contained within the gap and may have to be periodically processed. Figure 8.3-2 shows a possible design of a sliding electrical connection.

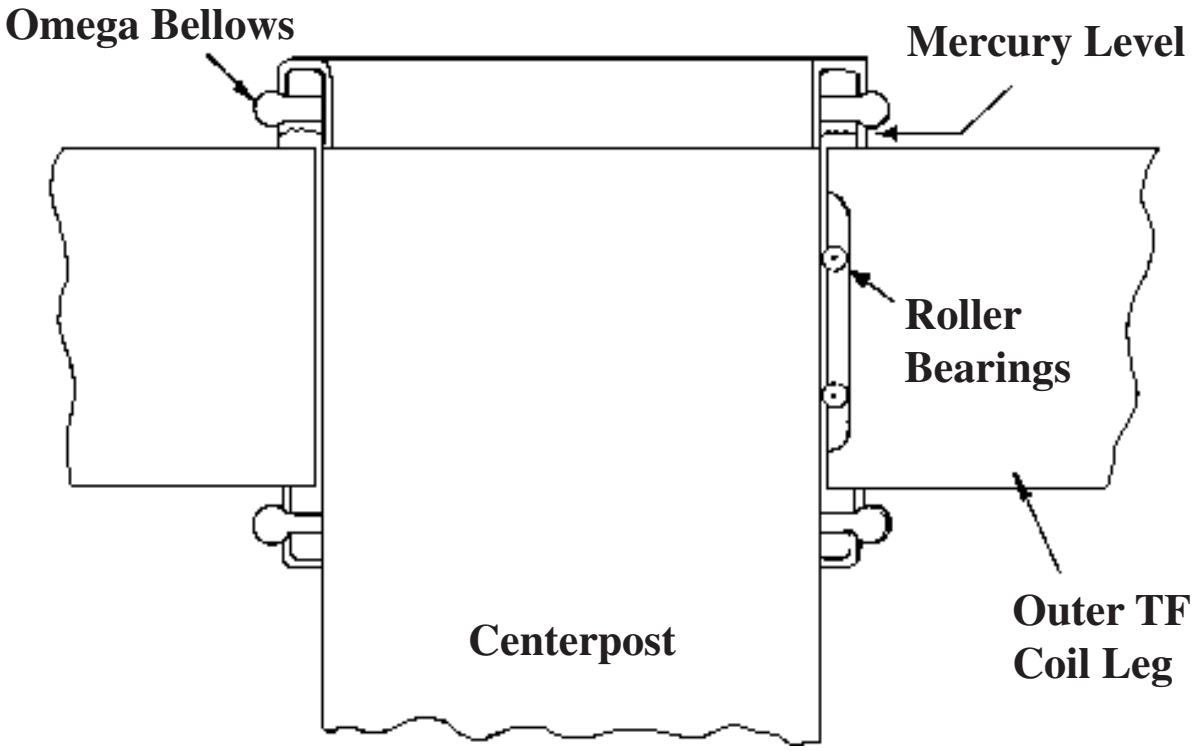

Figure 8.3-2. A possible design of a sliding electrical connection on the upper end of the center-post.

8.3.2.3. Fabrication of the center-post

In this design it is assumed that the center-post will be fabricated from the dispersion strengthened copper C15725. Present facilities for making dispersion-strengthened copper are limited to about a length of ∼2.5 m whereas the center-post is about 34 m long. However, there is no reason why larger pieces cannot be fabricated if appropriately sized heated pressure vessels can be provided.

Dispersion strengthened copper is made from a pure copper powder mixed with small quantities of AlO_2. A form is made of OFHC copper, the powder is then poured into the form and then heated while being subjected to a pressure of ∼10 MPa. The exact temperature and pressure values are proprietary and are not precisely known. Another method is called the internal oxidation technique used by SCM Corp. in producing GlidCop [19]. The patented process begins with melting a dilute solid solution alloy of copper and aluminum. The melt is atomized into powder and used in forms as described above. During heating, the aluminum in the alloy is selectively oxidized in-situ. The powder is then consolidated into fully dense shapes by one of several conventional metal working processes.

For making the center-post with the tubes in place, it would be necessary to pre-locate the tubes in the form prior to filling the form with the powder [20]. In this case, the tubes will also be made of dispersion-strengthened copper. The tubes can be shaped both in diameter and configuration, then fixed in position by dispersion-strengthened copper straps. It is possible that minor shifting of the tubes will occur during consolidation. This should not be a serious problem since copper has a very high thermal conductivity.

It would also be possible to fabricate the center-post in several sections. For example, the central portion can be fabricated separately, and each of the end portions separately. The three sections can then be diffusion bonded into one whole. Care will be needed to ensure that the tubes line up and that no distortion will occur at the interfaces.

The center-post can also be fabricated from other copper alloys, but the design would have to be different from that described above. For example, the use of concentric rings as proposed in Ref. [18] can be fabricated from other copper alloys. Center-Post shaping for minimizing ohmic heating will be more difficult to accomplish.

8.3.2.4. Conclusions

Based on these scoping calculations, the following conclusions have been reached regarding the calculations of the mechanical behavior of the center-post:

1. The compressive stresses caused by the magnetic field probably require the higher strength of dispersion-strengthened copper which has a higher electrical resistivity than pure copper.

2. The expansive forces on the outboard TF-coil legs cannot be reacted by the copper center-post. Either external clamping by the building structure or a rather strong structure inside the center-post is required to avoid excessive high tensile stresses in the copper.

3. Fabrication of the center-post can be envisaged using present technology in consolidating dispersion strengthened copper, assuming that sufficiently large ovens will be available. Alternatively, the center-post can be made in segments which are diffusion bonded together.

8.3.3. Design Implications of Copper and Copper Alloy Embrittlement

The design implications of a structural material which embrittles during neutron irradiation are very subtle. The issue is being addressed within ITER by the combined efforts of the Interim Structural Design Criteria and Material Properties Handbook Working Groups. An elaborate set of design guidelines and a material properties database have been published in draft form for austenitic stainless steel [Type 316L(N)] and is currently under review. With regard to copper and copper alloys, the current draft of the Handbook contains properties for Cu-Cr-Zr but not for pure copper or oxide-dispersion-strengthened copper (*e.g.,* GlidCop Al-15). Design rules have not yet been formulated for the use of copper and copper alloys in ITER. It should be noted, the "licensing" agencies (such as NRC) will ultimately develop or adopt the design codes for fusion power plants.

Given the status of the ITER design and material properties efforts, the approach taken in this assessment of the impact of copper embrittlement on the design of the center-post magnet for a low-aspect-ratio tokamak design is to parallel the rules developed for 316L(N) taking into account the similarities and differences between steel and copper embrittlement. In other words, design criteria will be established for copper alloys which preserve the same design margins or safety factors (SF) as have been established for 316L(N) for average (P_m) and local (P_l) primary membrane stresses, for primary bending stresses (P_b), for secondary stresses (Q) and for peak local stresses (F) in the region of cracks, notches, *etc.*

The operating conditions for both types of materials are restricted in this work based on the design applications. For ITER 316L(N), the nominal operating temperatures are

100–400 °C with short time excursions up to 500 °C. For this evaluation it is assumed that in order to maintain high enough electrical and thermal conductivity, the nominal operating temperature of the copper is in the range 0–100 °C, with short time excursions to higher temperatures possible. Also, to focus this section, only the properties of high purity copper (annealed) and GlidCop Al-15 [hot-isostatically-pressed (HIP)] are considered.

8.3.3.1. Effects of embrittlement on design criteria

Pure copper, GlidCop Al-15, and 316L(N) are all ductile materials at the beginning of life in a fusion environment. Conventional design rules (*e.g.,* ASME Boiler and Pressure Vessel Code [21]) may be used to establish temperature and stress limits to achieve the desired lifetime of a component. Although the strengths of these materials increase with radiation-induced hardening, the allowable loads must be determined based on the softer unirradiated properties to cover the beginning of life (BOL) operation. The design challenge is to demonstrate that these design-allowable loads lead to acceptable safety factors as the material hardens. This is clearly no problem with regard to strength as both the yield (YS) and ultimate tensile (UTS) strengths increase with neutron fluence. However, these strength increases cannot be relied on from a design perspective as short-term over-heating during off-normal events, as well as cycling during normal operation, can soften the irradiated material. Rather, the challenge is to demonstrate that the decrease of uniform elongation (UE) and local failure elongation [as measured by reduction in area (RA) in the neck region of a failed tensile specimen] due to embrittlement do not lead to unacceptable safety factors. Because ductility is not as recoverable with over-heating as the strength properties, the design-conservative approach of loss of ductility with no increase in strength is adopted for these materials.

For the materials of interest in the established temperature ranges, the uniform elongation drops to below 1% at neutron damage levels > 0.01 dpa for copper and copper alloys [22, 23] and ≥ 7 dpa for 316L(N) [24]. From a design viewpoint, both materials would be classified as brittle with such low values of uniform elongation. Clearly, the copper and copper alloys embrittle at much lower dpa values than the ITER 316L(N) steel. Also, 316L(N) has another advantage over copper. While the uniform elongation decreases significantly with dpa, the local failure elongation (as measured by RA) remains high, at least up to 10 dpa. This is important with regard to low-cycle fatigue strength and blunting of stress concentrations at crack tips. Although no direct RA data were found for irradiated copper and copper alloys, the decrease in total elongation (TE),

particularly for the dispersion-strengthened alloys (TE $\sim 2\%$ at ≥ 0.01 dpa), suggests that the local failure strain also decreases significantly with neutron exposure. Thus, copper-alloy embrittlement in a low-aspect-ratio tokamak presents two challenges above and beyond those for ITER 316L(N): the rate of embrittlement is much higher and both the uniform and local failure elongations decrease to very low values.

The approach to incorporating embrittlement into the center-post design criteria is to establish design acceptable stresses based on unirradiated properties and to insure that adequate design margins to failure are preserved as the material embrittles. If this is not the case, then either the design lifetime must be limited and/or the allowable stresses must be reduced until the design margins are satisfied. For the ITER 316L(N), it has been shown that the conventional design rules based on unirradiated properties lead to a minimum safety factor of 3 for primary membrane stresses (P_m) and a safety factor of 2 for local primary membrane plus primary bending stresses ($P_l + P_b$) even with irradiation embrittlement [25]. The safety margins for secondary stresses (Q) and peak stresses (F) have not yet been established for irradiated 316L(N), and thus will have to be treated separately for the copper alloys.

8.3.3.2. Design stress intensity

The design stress intensity (S_m) is a tabulated parameter in design codes for code-qualified structural materials. For ductile materials such as unirradiated copper and copper alloys, it is generally determined from

$$S_m \quad = \quad \text{Min}(2/3 S_{yd}, 1/3 S_{ud}) \tag{8.3-3}$$

where S_{yd} and S_{ud} are design yield and ultimate strengths based on minimum room temperature values and normalized average temperature dependence. For low temperature operation and simple design rules, S_m is sometimes listed as the design allowable stress with a limiting temperature of operation. For the more elaborate design rules, S_m is referred to as the design stress intensity and the rules include criteria for higher temperature application.

It is important to be specific with regard to material, tempering treatment, and component size when quoting a design stress intensity. The Metals Handbook [26] uses the UNS designations C10100 for Oxygen Free Electronic (OFE) copper and C10200 for Oxygen Free (OF) copper. The ASME Boiler and Pressure Code [21] has qualified C10200 as a low-temperature structural material. The S_m values for this material in the

"O60" temper condition are shown in Fig. 8.3-3. The limiting temperature of operation is listed as about 200 °C, because the tensile and creep-rupture strengths of this material decrease dramatically above this temperature. The material can be hardened (*e.g.,* H80 tempering condition) to produce significantly higher allowable stresses (*e.g.,* more than double up to 180 °C). However, the effects of this type of hardening are lost above 200 °C and it is more suitable for wires and small diameter tubes than for large complicated structures such as the center-post. Also, the ductility of hardened (*e.g.,* cold worked) copper is much lower than that of annealed copper in the irradiated condition. Thus, this strengthening mechanism is not considered. Rather, oxide-dispersion hardening is an appealing option if higher strength is desired up to higher operating temperatures. The design stress intensity of the commercial alloy GlidCop Al-15 (UNS C15715) [19] is also shown in Fig. 8.3-3. The particular values are for products produced by hot-isostatic-pressing (HIP) which may be a practical fabrication technique for the center-post. Beyond the 500 °C limit of the horizontal axis in Fig. 8.3-3, the GlidCop properties decrease linearly with temperature, unlike the pure copper properties which decrease significantly beyond 200 °C. At 100 °C, S_m = 37.4 MPa for pure copper (C10200 in the O60 temper) and 108 MPa for GlidCop Al-15 (HIP).

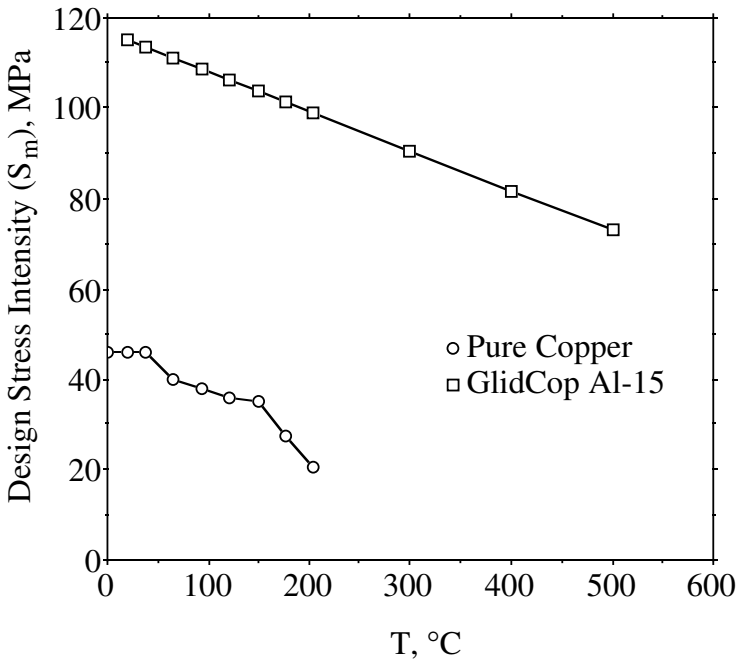

Figure 8.3-3. Design stress intensity (S_m) values for pure copper (C10200 in O60 temper) and GlidCop Al-15 (HIP) in the unirradiated condition.

8.3.3.3. Stress limits

The design stress intensity, along with other limiting parameters, is used to determine acceptable levels of average primary membrane stress (P_m), local primary membrane stress (P_l), primary bending stress (P_b), secondary stress (Q), and peak stress (F). Safety factors (SF) for each loading combination can be determined by ratioing the stress which causes failure to the allowable stress. These safety factors are explored as a function of decreasing ductility in the following. The average primary membrane stress (*e.g.,* wall-averaged hoop stress in a pressurized coolant tube) is limited by $P_m \leq S_m$. The safety factor for this type of loading is

$$SF_m \quad = \quad S_{ud}/P_m \tag{8.3-4}$$

and is always ≥ 3 for a material which hardens regardless of ductility loss. With the way that S_m is defined for unirradiated 316L(N), the SF_m varies from 3 to 4 within the temperature range of 100 to 400 °C. For irradiation-hardened 316L(N), the SF_m can be ≥ 5, but this is not taken advantage of because of the possible loss of hardening with cycling and temperature excursions. A similar situation exists for pure copper and GlidCop Al-15.

The design limit for primary bending stresses (*e.g.,* bending of a beam due to mechanical or electromagnetic moments) is given in the design codes as

$$P_l + P_b \quad \leq \quad K\, S_m\,, \tag{8.3-5}$$

where K is a shape factor for ductile materials (*e.g.,* $K = 1.5$ for a beam or plate with rectangular cross-section).

Two approaches have been used to account for the effects of irradiation-induced hardening on this limit. The first approach is to increase S_m with strength hardening and decrease K based on the loss of plastic ductility. This approach is not recommended because of the possibility of temperature-induced softening. The second approach is to define S_m and K based on unirradiated properties and to explore the effect of decreasing ductility, with no increase in strength, on the safety factor SF_{mb} for combined primary membrane and bending loads. In Ref. [25] it is shown that $2 \leq SF_{mb} \leq 4$ for 316L(N) within the temperature range of 100 to 400 °C. As the ductility drops to zero, the safety factor becomes 2 for all combinations of primary membrane plus bending loads as long as $P_b > 0$. Sample results are shown in Fig. 8.3-4 for 316L(N) at 160 °C. If the confidence level in the design is based on the minimum safety factor, then the embrittlement of the copper or copper alloy during irradiation will result in the same safety factor as the

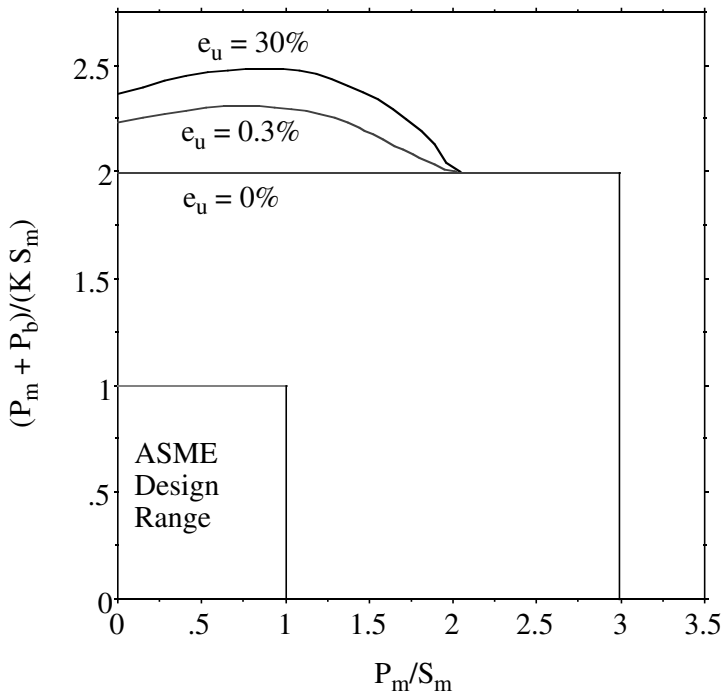

Figure 8.3-4. Safety factors for primary membrane plus bending loads as functions of primary membrane loads based on an elastic/linearly-plastic model. The assumed design properties correspond to those of unirradiated 316L(N) at 160 °C: S_{ud} = 440.1 MPa, S_{yd} = 163 MPa, S_m = 147 MPa, and e_u = 30%. A rectangular cross-section (K = 1.5) is assumed. The other two cases (e_u = 0.3% and e_u = 0%) are presented to show the effects of decreasing ductility on the safety factor.

minimum value accepted for 316L(N). Until some change is made in the design rules for ITER 316L(N), it is concluded that designing the center-post based on the unirradiated properties of the material will lead to acceptable safety factors for primary membrane and bending stresses as the material loses ductility due to irradiation hardening.

Secondary stresses (Q) such as thermal stresses are limited in combination with the primary stresses. The limit is designed to protect against local ratcheting of the material and fatigue damage, and is given by

$$P_l + P_b + Q \;\leq\; 3S_m\,. \tag{8.3-6}$$

However, as the uniform and total elongation drop below about 1%, this rule cannot be used. While ratcheting is not a problem for such a hardened material, low cycle fatigue may be. In particular, the fatigue damage is assumed to scale with the square of

the ratio of the unirradiated failure ductility to irradiated failure ductility. While these failure ductilities are supposed to be determined from RA measurements, very little data were found in the literature for the reduction in area as a function of neutron fluence. For the sake of a numerical example, though, the ratio of the total elongations is used. For annealed pure copper irradiated and tested at about 100 °C, the total elongation decreases from about 50% in the unirradiated condition to about 10% at 1 dpa. Thus, the reduction in low cycle fatigue life is estimated to be a factor of about 25 due to irradiation embrittlement. For GlidCop Al-15, the ratios of total elongations can be as much as a factor of 10, leading to a reduction in low cycle fatigue life of as much as 100. These examples both illustrate the potential reduction in low cycle fatigue life for irradiated copper and copper alloys, as well as emphasize the need for either fatigue data on irradiated samples and/or reduction-in-area measurements for irradiated tensile specimens.

The stress limit criterion on the peak stress (F) in the area of cracks and notches is designed to guard against rapid or instantaneous crack growth leading to failure under static loading conditions. It is expressed as a sum of all of the stresses:

$$P_l + P_b + Q + FS_l \,, \tag{8.3-7}$$

where S_l is a complicated function of a number of parameters and properties, including the fracture toughness. Although no fracture toughness data were found for irradiated copper in the literature reviewed, based on the decreases in both uniform and total elongation, it is anticipated that there will be a significant reduction in fracture toughness and that this reduction may result in further limitations on P_m, P_l, P_b and Q.

In addition to fatigue considerations which represent time-dependent phenomena, rules are available to protect against creep rupture. However, if the operating temperature is maintained to $\leq$100 °C for the center-post design, then this high temperature phenomenon should not limit the operating stresses beyond the limits already imposed.

In summary, the embrittlement of copper and copper alloys with neutron exposure may introduce further limitations on design allowable primary and secondary stresses because of reduction in low-cycle fatigue life and because of reduction in fracture toughness with ductility loss. To assess the magnitudes of these impacts, it is important to have low cycle fatigue data and/or reduction-in-area data for irradiated samples, as well as fracture toughness data. These limitations on allowable design stresses would have to be compared to anticipated operating stresses. For very low operating stresses and/or very short design lifetime, the additional limitations may not pose a problem.

8.3.3.4. Deformation limits

In addition to the traditional stress limits, deformation limits may pose additional constraints to the design-allowable operating stresses. Such limits are highly design dependent. Generic ones which have been developed for scoping studies are: $\leq$5% volumetric swelling, $\leq$5% irradiation creep, and $\leq$1% thermal creep. For operating temperatures $\leq$100 °C, none of these should be design-life-limiting beyond limits imposed by the effects of transmutation products on the electrical conductivity. However, the swelling criterion needs to be closely evaluated in the light of possible transient overheating events. With enough transmutation helium present, 5% volumetric swelling could be achieved during short-time, high-temperature transients. These He bubbles would essentially be frozen into the material upon return to the low operating temperatures.

8.3.3.5. Limits based on high-strain-rate events

Most of the above design limits assume strain-rate-independent properties and operating conditions. High strain rate events (*e.g.,* disruptions acting on the first wall or divertor) could cause problems with embrittled irradiated material. To assess this issue, fracture toughness data under high strain rate loading should be gathered for irradiated copper and copper alloys. For scoping tests, the Charpy impact test may be used.

8.3.3.6. Summary

Developing design criteria for materials which are ductile in the unirradiated condition, but embrittle significantly with neutron exposure, is an evolving art. The criteria which have been developed within the ITER design and materials groups for 316L(N) stainless steel have been used to guide the information presented in this section. While both 316L(N) and copper alloys increase in strength and decrease in uniform elongation with neutron exposure, the copper alloys present a particular challenge because of their faster rate of embrittlement and their decrease in local failure strain, as well as uniform elongation. The approach to developing design criteria is based on using the softer unirradiated properties to set operating stress limits and then to track the factors of safety with fluence to determine at what level of dpa embrittlement causes unacceptable decreases in safety factors or design margins. This was done explicitly for primary membrane and bending stresses, for which it was concluded that copper embrittlement would not be a problem. However, it was established that the embrittlement may result

in either a decrease in lifetime or a decrease in allowable operating stresses based on low cycle fatigue considerations, rapid crack growth under static loading and crack growth under high strain rate loading. To assess the impact of these possible design restrictions, additional data need to be gathered or generated on low cycle fatigue and/or local tensile failure strain for irradiated copper, as well as fracture toughness for a wide range of strain rates for irradiated copper.

Material properties and design limits alone do not preclude the use of a material in a fusion application such as the center-post of a low-aspect-ratio tokamak. These must be compared to anticipated operating stresses. If the operating stresses are low enough and/or the design lifetime is short enough, then the design margins may be high enough to justify the use of materials such as copper and copper alloys even with their loss in ductility with neutron exposure.

8.3.4. TF-Coil Power Supply and Busbar

8.3.4.1. Power supply

The use of a single-turn TF coil system raises several concerns regarding power supplies that can provide high current at low voltage, and regarding the potentially large losses in lead wires and joints. The TF coils of low-aspect-ratio tokamak devices are different from smaller normal conducting magnets in that they have a large ratio of stored energy to dissipated power. This is a consequence of the large size of the magnet, since the energy scales with the cube of the linear size while the dissipated power scales with the square of the linear size (for comparable fields). This fact may have a large effect on the choice of the power supply. For the low-aspect-ratio tokamak strawman, the energy stored is about 9 GJ, while the dissipated power is about 1,500 MW. It is straightforward to determine the time constant for the system,

$$\tau \ = \frac{L}{R} \ = \ \frac{2E}{P} \tag{8.3-8}$$

where L is the inductance, R is the resistance, E is the energy, and P is the resistive power. For the low-aspect-ratio tokamak strawman, $\tau \sim 10$ s.

If fully-rectified 60 Hz is used as the driver, the resulting ripple is $\lesssim$0.1% (without any filtering or regulation). Therefore, there is no need for regulation, and the power supply basically is reduced to a transformer and one or several diodes, using the line power as the driver. Typical 25-kA transformers are large and heavy, but inexpensive.

Each power supply module has a 25-kA capability, driving its own busbar (either normal conducting or superconducting, as described above). For the strawman, there are 1,200 power supplies. Due to the simplicity of the power supply, the cost of the power conditioning equipment is not a dominant cost of the device. The system looks very similar to those used in large scale electrolytic processes for the production of aluminum, although with much larger scale.

Alternatively, a switching power supply could be used at higher frequencies, reducing the size of the transformer but increasing the cost of the driver. These switching power supplies have been developed recently to deliver very high specific power, on the order of 3 MW/m^3. Estimated costs for small units (2 kW) are \$750. The power supplies include protection, stability and regulation. Therefore, if 150,000 of these units are used, the maximum cost of the power supply would be \$110M. Larger units are being developed, and advantages of scale, together with larger units with combined controls, could reduce the cost of the power supply to less than \$50M. This power supply design is much more compact but more expensive than the 60-Hz transformers. Because of the reduced size, it would be possible to place the power supply closer to the reactor, decreasing the required busbar length and associated costs.

8.3.4.2. Busbar concerns

There is a tradeoff between the size of the busbar and the dissipated power, for room temperature busbar. This tradeoff is shown in Figure 8.3-5 as a function of the cross sectional area of a room temperature copper busbar. Very large costs are associated with the busbar and dissipated power. It is assumed that the copper in the busbar cost is \$20/kg and that the busbar is 50 m long. The cost of the electricity is 90 mills/kWh, the plant operates for 30 years with a 80% capacity and the interest rate is 5%. Means of decreasing the costs are analyzed in the following sections.

Cryogenic busbar. There are large decreases in the resistivity of materials with decreasing temperature. These advantages, however, are lost in the case of magnets due to the substantial magnetoresistivity of most materials. However, for busbars with small magnetic fields, it is possible to obtain large decrements in power dissipation (ohmic and cryogenic losses) by decreasing the temperature of operation of the busbar, as long as the busbar is broken into a large number of current leads and each lead is placed next to other ones with opposite currents, in order to decrease the value of the magnetic field generated by the leads. Concentric leads, of course, satisfy the latter requirement. The

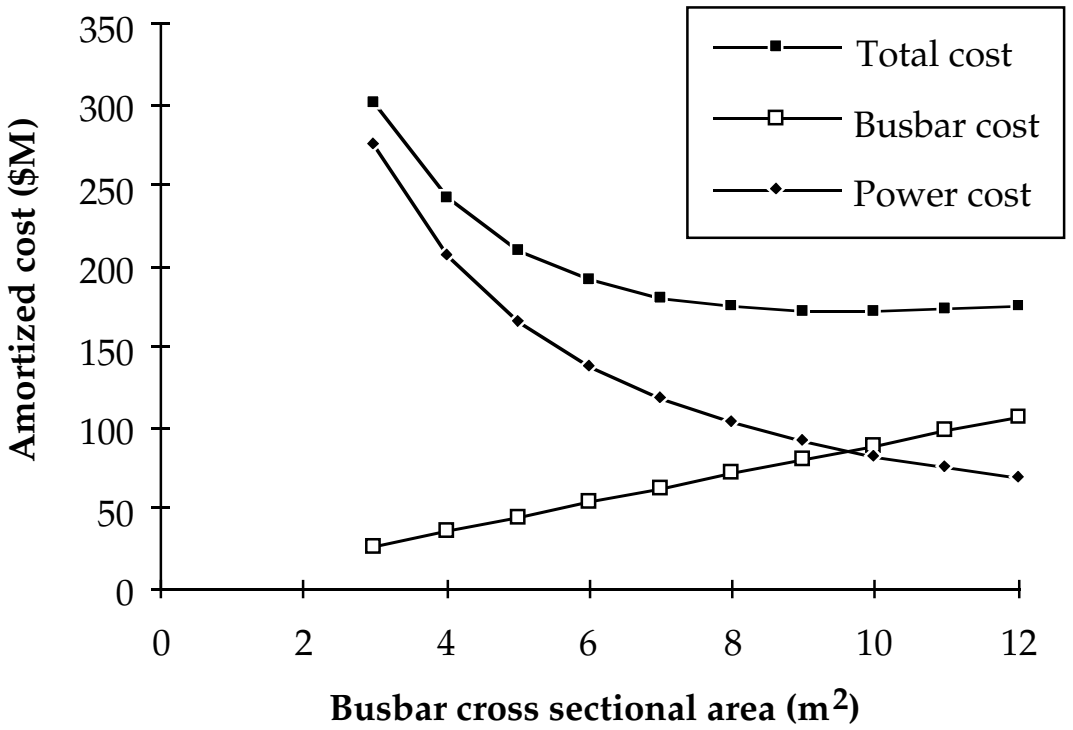

Figure 8.3-5. Amortized costs of busbar and power as a function of busbar area.

largest gains are obtained at temperatures in the range of 20 to 90 K. However, as shown in the next section, it is possible to have superconducting leads at these temperatures, and therefore we only analyze that case.

High-T_c superconducting busbar. Work in progress at MIT with Hoechst, Los Alamos, American Superconductor, and others indicate that superconducting current leads operating at 77 K (liquid nitrogen) can be manufactured. A collaboration between MIT and Hoechst in Frankfurth, Germany, has tested current leads that, at 77 K, can carry up to 16 kA at a current density of 1.5 kA/cm^2 (at self-field). Figure 8.3-6 shows the voltage per unit length of a 75-mm outer diameter (OD) hollow cylinders (5 mm thick), tested both at 77 K and at 66 K (obtained by pumping on liquid nitrogen). The maximum current of 16 kA is due to power supply limitations.

The resistive losses of the silver/superconductor joints of the same sample was measured to be less than 0.4 mW. The specific, resistive loss of the joints is about 2 mW/cm^2. For the current leads that are being discussed, a joint area of about 250 cm^2 is feasible by making the conducting region 10 cm long.

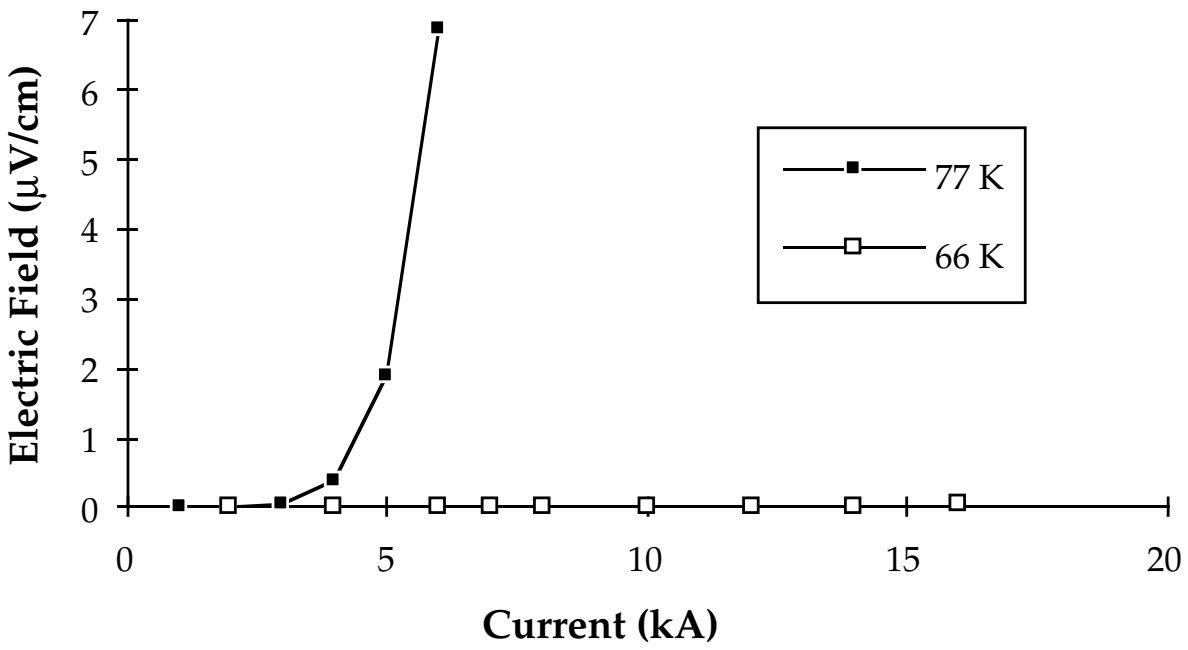

Figure 8.3-6. Electric field of high-T_c Superconductor vs current.

Figure 8.3-7 shows a schematic diagram of the analyzed joint. Hoechst together with MIT have developed reliable metallurgical bonds between the high-temperature superconductor and the silver contacts. For a 50-m busbar length, the power dissipated in the superconducting busbar is 150 kW, with a room temperature refrigeration of about 1 MW. The dissipation in the joints between the superconductor and the copper leads is minimum.

The present day cost of the high temperature superconductor current leads (hollow cylinders), offered commercially by Hoechst, is \$500 for a tube that is 0.4 m long. The low-aspect-ratio tokamak strawman requires about 30 MA, and with 25 kA busbar current, 1,200 current lead pairs are needed. The large number of current lead pairs is also needed in order to minimize the self field of the busbar.

In collaboration with Hoechst it has been determined that the hollow cylinders of 2212 BSCCO can be built with lengths on the order of 8 m (30 ft) for about twice the unit price of the 0.4-m lead (the bulk of the cost being the setup/testing time). Several of these cylinders can be connected in series in order to span the distance between the power supply and the nuclear island. Currently, the superconducting leads are being investigated as a means of carrying the current from the generator to the transformer in present-day power stations.

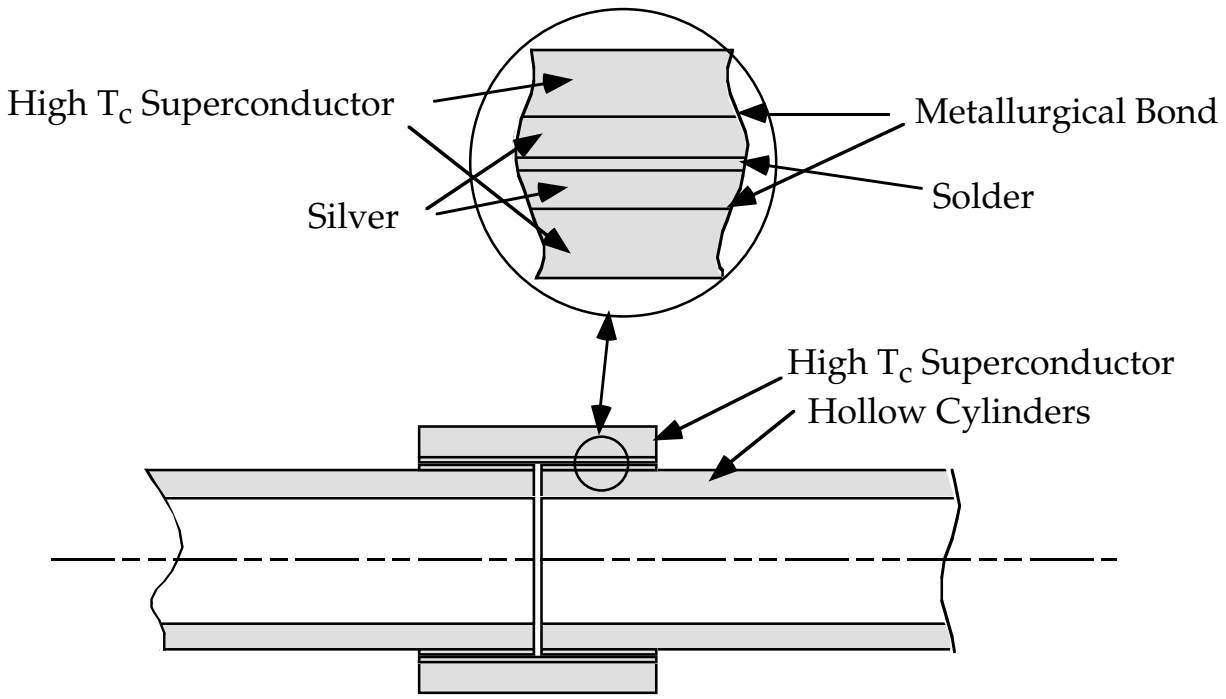

Figure 8.3-7. Schematic diagram of a joint, showing metallurgical and solder bonds.

The cost of the busbar is on the order of \$1.2 M/m, if 0.4 m long sections are used, or \$60 M for a 50-m busbar length. These tubes are commercially available now. If 8-m tubes can be manufactured, then the cost would be \$300 k/m, or \$15M for a 50-m-long busbar.

In order to minimize self-field, conductors with opposite currents need to be placed near each other. The case that was studied had concentric hollow cylinders, with the magnetic fields exclusively in the region between the tubes. The space between the tubes is used for coolant. The evaporation of liquid nitrogen was determined to be several liters per hour of operation. The overall size of the bus bar, even with the gaps for liquid nitrogen, is much smaller than that for normal conducting busbars. Also, the power dissipation is virtually eliminated.

8.3.5. Shielding Options, Radiation Effects, and Activation

This section covers the neutronics, activation, and shielding requirements for the low-aspect-ratio tokamak power plant. A scoping analysis was performed for a preliminary configuration in order to guide the design toward a final configuration that satisfies all the top level requirements developed by the Starlite team for U.S. fusion power plants. Generally, U.S. designs emphasize safety and environmental aspects of fusion, providing a strong incentive to generate low rad-waste, not greater than Class C.

The center-post presents important design problems to designers. Therefore, most of the neutronics, activation, and shielding activities were devoted to the center-post and little attention was given to the outboard and divertor regions. Due to the severe radiation environment, it is important to identify potential radiation-induced effects and failure mechanisms so that the center-post lifetime could be reasonably predicted. In addition, changes in the electrical resistivity of the center-post and the volume of waste produced have dramatic impact on the design.

In order to identify the potential neutronics-related issues, we first considered a preliminary case with no intervening shield between the first wall and the center-post. This center-post is this configuration has a minimum diameter of 0.874 m composed of 70% dispersion-strengthened copper alloy with 0.25 wt.% aluminum (dispersion-strengthened GlidCop Al25) and cooled with 30% water at an average copper temperature of 75 °C. The maximum temperature of copper is kept at roughly 110 °C. The machine planned operation is 40 y (30 full power years, FPY) with an average neutron wall loading of 4.1 MW/m^2. The peak inboard wall loading occurs at the mid-plane at a value of 3.6 MW/m^2. The total height of the center-post for this preliminary case is 16 m and no inboard shield was placed between the plasma and coil, except for a 1.4 cm thick heat removal surface.

The neutronics model employed the 1-D transport code ONEDANT [27] with the P3 Legendre expansion for the scattering cross section and the S8 angular quadrature set. The associated 46 neutron and 21 gamma group cross section library was derived from the ENDF/B-V evaluation. The transport problem is modeled in toroidal cylindrical geometry around the machine axis and calculations are carried out to investigate the various responses of interest. For the center-post, there are concerns with mechanical degradation of copper due to radiation damage, increase in copper resistivity due to neutron-induced transmutations, and activation of copper leading to an unacceptable level of radioactive waste. The results reported below illustrate how severe the radiation damage and activation levels are for the unshielded center-post.

8.3.5.1. Waste-disposal requirements

The goals and objectives developed by the Starlite team for the fusion power plants clearly state that all designs must demonstrate that fusion is a safe, environmentally attractive, and licensable power source that is ready for commercialization at an economically superior total cost. This led to a set of requirements on materials and technology choices and design specifications. Among these requirements, fusion plants should generate only low-level waste and all waste can be recycled and/or disposed of at an acceptable level.

The safety and environmental requirements mandates that all in-vessel components generate no radioactive waste greater than Class-C level. Vanadium alloys and low-activation ferritic steels have the potential of meeting these requirements if employed for first-wall, blanket, and shield operating at a moderately high fluence of 12 MWy/m^2 or less.

Fusion power plants in U.S. will probably be licensed and regulated by the Nuclear Regulatory Commission (NRC) and other environmental agencies. Thus far, the NRC guidelines for Class C waste currently documented in the 10CFR61 report [28] were basically developed for nuclear waste generated by medical and industrial facilities, and fission power plants. Therefore, NRC regulations do not contain some materials that may be of interest to fusion, such as V, W, Si, Sn, ..., *etc.* A complete list of rad-waste limits specifically for commercial fusion plants will be eventually developed or adopted by NRC. Several years ago, Fetter [29] used and modified the NRC methodology to develop waste-disposal limits for a wide range of radionuclides which are of interest to fusion researchers. He also used different conversion factors and transfer coefficients and limited the dose to the whole body rather than to a single organ, as in NRC. In addition, he used his work to re-evaluate the isotopes that have already NRC limits and, in some cases, arrived at different limits than those of NRC.

Development of waste-disposal limits is outside the scope of this research. Therefore, the philosophy adopted by our Starlite team is that all the in-vessel components should meet both NRC and Fetter's limits for Class-C waste. In fact, all previous ARIES designs have adopted the same philosophy and we plan to continue imposing both limits on all ARIES/Starlite designs until NRC develops official guidelines for fusion plants.

For the low-aspect-ratio tokamak design under consideration, the activation analysis has indicated that the unshielded center-post will not qualify as Class C waste under neither NRC nor Fetter's waste-disposal limits, unless the center-post lifetime is limited

to 0.12 FPY (∼2 calendar months). To prolong the center-post lifetime, a 20–30-cm thick inboard shield is needed for 4 years or more of operation. The option of replacing the unshielded center-post every 2 months is not acceptable for power plants due to the loss in availability and the generation of large amount of radioactive waste. The unshielded center-post option could, however, be acceptable for experimental devices operating at much lower fluences and not bound by the Class C waste requirement. In addition, this shield helps improve the design in many aspects (Sec. 8.3.1). Hence, the shielded center-post is the reference design for the low-aspect-ratio tokamak machine.

The low-aspect-ratio tokamak machines will generate more rad-waste compared to conventional-aspect-ratio tokamaks. The low-aspect-ratio tokamak designs are highly elongated (30 m for low-aspect-ratio tokamak compared to <15 m for conventional-aspect-ratio tokamaks) resulting in a much larger waste stream for the low-aspect-ratio tokamak in-vessel components, especially when considering the disposal of the massive center-post (∼300 tonnes) every ∼4 years. It is true that recycling helps reduce the waste, but this will come at a much larger cost for the low-aspect-ratio tokamak machines.

8.3.5.2. Waste-disposal rating analysis

The activation calculations were conducted using the DKR-ICF computer code [30] with activation cross sections taken from the USACT93 [31] library and radial neutron flux distribution generated by the transport code ONEDANT. The neutron transmutation data used is in a 46-group structure format. The center-post activation results were utilized in the rad-waste classification. The rad-waste of all alloys were evaluated according to both NRC 10CFR61 [28] and Fetter [29] waste disposal concentration limits. The copper alloy used in the activation analysis is the dispersion-strengthened alloy GlidCop Al25 and the poloidal average neutron wall loading over the center-post is 2.5 MW/m^2. The Class-C waste-disposal ratings of the center-post as a function of operation time are as shown in Table 8.3-II.

In order to be qualified for Class-C waste disposal, the waste-disposal rating (WDR) should be below unity. As shown in the table, the center-post will not qualify for disposal as Class-C waste for operating times longer than a few weeks to a few months, regardless of the limits used. Note that ^{63}Ni (half-life of 100 y) dominates the WDR considering the NRC limits. Longer cooling off periods of 10 y or more will not change the WDR for such long lived radionuclides. The isotope ^{63}Ni is produced directly from copper while Ag is an impurity and Al is an additive to the GlidCop alloy. Since ^{63}Ni is generated from copper, using different copper alloys would not make a difference in the WDR. Reducing

Table 8.3-II.
Class-C Waste-Disposal Rating[(a)] for
the Dispersion-Strengthened Glidcop Al25 Center-Post
(2.5 MW/m^2 and 1 y Cooling-Off Period)

Time of Operation	Fetter Limits	NRC Limits
6 months	2.64[(b)]	4.11
1 year	4.94[(c)]	8.53
3 years	12.2[(d)]	29.1

(a)Dominant isotope is given in parenthesis.

(b)Breakdown: 2.56 (^{108m}Ag) and 0.081 (^{26}Al).

(c)Breakdown: 4.76 (^{108m}Ag) and 0.16 (^{26}Al).

(d)Breakdown: 11.6 (^{108m}Ag) and 0.48 (^{26}Al).

the silver content in the copper alloy (currently at 0.002 w/o) by an order of magnitude would allow for the disposal of the center-post after 1 FPY as Class-C waste according to Fetter's limits only. Table 8.3-II indicates that the NRC limits are more stringent and will thus be used to determine the center-post lifetime and shielding requirements. In order to dispose of the center-post as Class C waste, the center-post should be subjected to a fluence $\lesssim$0.3 MWy/m^2. Since the economics mandate operating at high neutron wall loading, it is therefore necessary to either limit the center-post lifetime to 0.12 full power year (FPY), or shield the center-post for longer life. It was estimated that in order to replace the center-post every 3 FPY (same as blanket) or more, the WDR should drop by a factor of >30. This could be achieved by placing 20 to 30 cm of shield between the plasma and center-post. The shielded center-post will thus have an end-of-life fluence of 0.3 MWy/m^2 or less.

To conclude, only two options seem to satisfy the Class-C waste requirement. The first option is to limit the lifetime of the unshielded center-post to 0.12 FPY. The second option is to shield the center-post with 20 to 30 cm thick shield to prolong the lifetime to 3 FPY or more. Both options will alleviate most of the radiation damage problems en-

countered in the highly irradiated center-post. However, the unshielded case is penalized for generating a lot more rad-waste and having longer machine down time (*i.e.,* lower availability).

8.3.5.3. Irradiation Effects

The lifetime of the various components is determined by the design criteria and requirements developed by the Starlite team for U.S. commercial power plants. These requirements include structural integrity, Class C waste, and radiation damage. The high radiation environment in the low-aspect-ratio tokamak machine mandates that some of the in-vessel components need frequent replacement during the 40-y plant life due to radiation damage considerations. These components are the blanket, divertor, and center-post. The blanket (and divertor) useful lifetime is determined by the integrity of the main structural material. The criterion adopted in this study is that no more than 150 dpa is desirable for ferritic steel and vanadium structures. This corresponds to an end-of-life fluence at ∼12 MWy/m^2 for a typical first wall neutron spectrum. This means that for an outboard neutron wall loading of 4–6 MW/m^2 the blanket (and divertor) lifetime is in the order of 2–3 operational years at full power.

Four radiation effects are likely to degrade the performance and thus limit the life of the center-post, namely the embrittlement of copper, changes in copper resistivity due to transmutations, neutron-induced swelling, and activation of copper leading to high level waste. At present, the dominant life limiting factor for the center-post is found to be the activation of copper. The highly irradiated unshielded center-post appears to have a lifetime of 2 months, limited by the Class C waste disposal requirement. To prolong the coil life and thus increase the plant availability, the center-post should be shielded. It is estimated that a 20–30 cm shield would allow the center-post to function for 4 years or more.

Radiation-induced changes in copper resistivity Neutron irradiation will increase the copper resistivity due to the production of neutron-induced transmutations, defects, and dislocations. The resistivity effect due to radiation damage is small compared to that due to transmutation [32] because of the fact that a large fraction of the defect-induced resistivity is expected to anneal out at the operating temperature of the center-post (∼100 °C). Moreover, the defect-induced resistivity saturates at low fluence while the transmutation-induced resistivity scales somewhat linearly with fluence. Increasing resistivity with time means increasing power dissipation in the coil, leading to higher

recirculation power, lower net efficiency, and a larger machine required to offset the effects of higher recirculating power and lower net thermal efficiency.

At any instant of time, the two stable isotopes of copper (69.2% ^{63}Cu and 30.8% ^{65}Cu) interact with neutrons and give rise to transmutation products. The reactions of interest are Cu(n,H)Ni, Cu(n,α)Co, Cu(n,γ), and Cu(n,2n). The last two reactions produce unstable copper isotopes that β decays to Zn and Ni stable isotopes. The time-dependent inventory of both stable and unstable Ni, Co, and Zn isotopes is computed using the activation code DKR-ICF. After 0.12 FPY (the maximum lifetime allowed for the unshielded center-post to meet Class-C waste-disposal limits), the peak and average nuclide productions are listed in Table 8.3-III. The peak values represent the maximum values obtained at the center-post plasma facing surface having a peak wall loading of 3.6 MW/m^2. The average values are calculated for an average wall loading of 2.5 MW/m^2 and averaged radially over the center-post assuming a radius of 0.51 m.

The inventory of transmutations that is used to calculate the change in the center-post copper resistivity should be based on the average value, not on the peak. The average value is quite lower (factor of $\sim$6) than the peak which occurs at the mid-plane outermost layer of the center-post. The difference is due to the exponential attenuation of the neutron flux with radial distance through the coil and the vertical drop of the neutron wall loading over the height of the center-post. As shown later, the outer-most layer of the center-post exhibits a large inventory of ^{62}Ni, ^{64}Ni and Co produced by (n,2n) and (n,α) reactions which have threshold energies of 9 and 5 MeV, respectively. These reactions decrease rapidly within the coil. The resulting resistivity change in the copper

Table 8.3-III.
Amount of Transmutation Products (appm) Produced in the Unshielded Center-Post after 0.12 FPY

Nuclide	Peak	Average
Ni	2,108	360
Co	23.6	2.6
Zn	1,258	259

conductor can then be computed from the transmutations using a linear combination of the induced resistivity from the different elements as given by the relation:

$$\rho \;=\; \rho_{Cu} + \Sigma_i \rho_i A_i \,, \tag{8.3-9}$$

where ρ_i and A_i are the specific resistivity per atom percent and the atom percentage of the transmutation product i, respectively. The room temperature resistivity of copper and specific resistivities of Ni, Co, and Zn are 1.71×10^{-8}, 1.12×10^{-8}, 6.4×10^{-8}, 3×10^{-9} Ω-m, respectively [33].

The percentage increases in copper resistivity due to Ni, Co and Zn transmutations are listed in Table 8.3-IV. Nickel has the highest impact on copper resistivity followed by Zn and then Co. The average change in copper resistivity amounts to ∼3% implying that the power dissipation in the unshielded center-post due to transmutation-induced resistivity is small compared to the intrinsic ohmic losses in the center-post. The same conclusion holds true for the case of shielded center-post which is subjected to ∼0.3 MWy/m^2 fluence with a much softer neutron spectrum. The softer spectrum will result in a significant reduction in the high energy neutron-induced transmutations generated by the (n,2n) and (n,α) reactions. Thus, the shielded center-post will experience even lower change ($< 3\%$) in resistivity due to transmutations.

Table 8.3-V gives the detailed nuclide (impurity) production for the unshielded center-post. Since the nuclide production is given per unit fluence, the peak values are only representative of surface values (local values) and the average values are representative of values averaged over the total center-post thickness.

Table 8.3-IV.
Increase in Copper Resistivity of Unshielded Center-Post At 0.12 FPY

Nuclide	Peak	Average
Ni	13.8%	2.36%
Co	0.88%	0.1%
Zn	2.21%	0.45%

Table 8.3-V.
Nuclide Production (appm per MW-y/m^2) For Unshielded Center-Post

Nuclide	Peak	Average
^{60}Ni	2.7	0.4
^{61}Ni	6.6	0.6
^{62}Ni	1,312	203
^{63}Ni	262	47
^{64}Ni	3,297	937
Total **Ni**	**4,880**	**1,190**
^{59}Co	19.6	3.0
^{60}Co	35.1	5.6
Total **Co**	**54.7**	**8.6**
^{64}Zn	1,929	550
^{65}Zn	7	1.0
^{66}Zn	974	306.5
^{67}Zn	3	0.6
Total **Zn**	**2,913**	**858**

Atomic displacement in copper. There is serious concern over ductility degradation of the copper conductor under irradiation. The dispersion-strengthened GlidCop Al25 alloy proposed for the center-post undergoes rapid radiation hardening and loss of ductility at irradiation temperatures below 200 °C. Recent irradiation data showed rapid embrittlement of all copper alloys and complete loss of work hardening by 0.1 dpa [34]. The 0.1 dpa is reached for the unshielded center-post after one day of operation. For longer times of operation, the copper will be extremely brittle. Thus, the copper will have no structural integrity and design rules for brittle material should be used in designing the center-post. The radiation damage to the unshielded center-post is given in Table 8.3-VI for an arbitrary operation time of 1 FPY. The peak values are evaluated at the mid-plane for a peak inboard wall loading of 3.6 MW/m^2. The average values are 4 to 8 times lower than the peak. This reduction is due to the radial attenuation of the neutron flux over the 50 cm thick center-post and the vertical drop in wall loading over the inboard side. At 0.12 FPY, the peak value is 6 dpa for an unshielded center-post. Using a 20–30-cm-thick shield to protect the center-post will result in a peak value slightly lower than 6 dpa for 3 FPY. Other designs comprising different materials and using different data libraries and geometric models may produce different neutron spectra and different levels of radiation damage than the values reported in Table 8.3-V.

Table 8.3-VI.
Radiation Damage To Unshielded Center-Post

	Peak	Average[(a)]
Neutron wall loading (MW/m^2)	3.6	2.5
Atomic displacement (dpa/FPY)	48	8
Helium production (appm/FPY)	540	130
Hydrogen production (appm/FPY)	2,840	330
Nuclear heating	100 MW/m^3	160 MW

[(a)] For a homogeneous mixture of copper and water coolant.

Present knowledge of the annealing process indicates that a significant fraction of the radiation damage in the copper alloys could be removed by periodic annealing at 200 to 300 °C for a few hours. However, this might not be feasible for power plants. Periodic annealing for a few hours after each day of operation (upon reaching 0.1 dpa) will certainly lower the availability of the system. Continuous annealing is also unacceptable due to the increase in copper resistivity, neutron-induced swelling, and coolant corrosion at high operation temperature (200 to 300 °C).

Swelling of copper. Experimental data shows a rapid increase in the GlidCop swelling rate in the 100 to 250 °C temperature range of interest (Sec. 8.3.3). Higher temperature swelling behavior is not relevant to this low-aspect-ratio tokamak design. Table 8.3-VII lists the swelling rates at various temperatures and the peak/average swelling for an arbitrary operation time of 1 FPY. The peak swelling occurs at the mid-plane where the wall loading peaks at 3.6 MW/m^2. The average value is a factor of 6 lower than the peak. At 0.12 FPY, the peak swelling is <2%. The shielded center-post should have lower swelling rate. It is recommended to keep the maximum temperature below 180 °C to limit the swelling of copper.

Table 8.3-VII.
Neutron-Induced Swelling In Dispersion-Strengthened GlidCop
For Unshielded Center-Post

Operating Temperature	Swelling Rate	Peak Swelling	Average Swelling
<180 °C	<0.019%/dpa	1%	0.16%
220 °C	0.3%/dpa	14%	2.5%
250 °C	0.5%/dpa	24%	4.2%

8.3.5.4. Outboard shield

The need for water coolant for the center-post will most likely exclude the use of liquid lithium as a breeder for the outboard blanket of the low-aspect-ratio tokamak machine. Serious safety concerns arise when large amounts of Li and water coexist in a single machine. While a multiple-barrier approach could be applied to lessen the safety concerns, detailed assessments will be needed to demonstrate the ability to meet the requirement for no evacuation at the site boundary following any credible accident.

Other candidate breeders are lead-lithium, FLiBe, or solid breeders. The later will most likely requires beryllium multiplier to achieve tritium self-sufficiency. A 50-cm thick space is reserved on the outboard side for a blanket which is followed by a shield, and then a vacuum vessel . The shield should be sized to mainly protect the vacuum vessel and ensure that the neutron-induced helium production does not exceed 0.1 appm at the vacuum vessel. For costing evaluation, the systems code employed the ARIES-II outboard Li/V blanket (although it may be incompatible with the water cooled center-post) and the modified shield and vacuum vessel designs. The system has an overall neutron energy multiplication of 1.36 and a gross thermal efficiency of 46%.

8.3.5.5. Conclusions

Radiation-induced effects have a major impact on the center-post design of the low-aspect-ratio tokamak power plant. At present, the lifetime of the center-post appears to be limited by the Class-C waste-disposal requirements. As a consequence, the lifetime of the unshielded center-post is limited to 0.12 FPY (for a fluence of 0.3 MWy/m^2) or the center-post must be protected with 20–30 cm of shield. Since it is not feasible to replace 100 tonnes of copper every 2 months, the center-post should be shielded to prolong the lifetime to 4 years or more, reduce the cumulative rad-waste and replacement cost, increase the system availability and alleviate most of the center-post radiation damage problems.

We have assessed the effects of neutron fluence on conductor resistivity, swelling, and atomic displacement. The Ni and Zn transmutations will continue to build up and the effect on copper resistivity could be significant. For example, after one FPY operation without an inboard shield, 0.3 at.% Ni and 0.1 at.% Zn would contribute 25% additional ohmic losses. Even though the radiation-induced swelling and changes to copper resistivity due to transmutations are small at 0.3 MWy/m^2, there is a serious concern on the ductility degradation and the consequences of the high atomic displacement on the

conductor strength. The copper will embrittle quite rapidly at 0.1 dpa which is reached after one day of operation for the unshielded center-post and after 1–2 months for the shielded center-post. Designing a center-post with extremely brittle copper alloy will be a challenging engineering task.

The shielded center-post is our reference design for the low-aspect-ratio tokamak power plant. The inboard shield helps improve the design in many aspects. The shield can be used to add mechanical support for the center-post (Sec. 8.3.2). The nuclear heating ($\sim$150 MW) can be removed as useful heat from the shield (instead of being dumped at low temperature) and converted into electricity, reducing the center-post thermal hydraulic problems. The shield alleviates most of the center-post radiation damage problems and helps tremendously to reduce the rad-waste stream, replacement cost and change-out frequency, and increase the availability of the machine. Overall, the center-post shield improves the low-aspect-ratio tokamak design significantly.

8.3.6. Blanket and Power Conversion Assessment

8.3.6.1. First wall and blanket design options

The selection of the blanket option for the low-aspect-ratio tokamak design is even more complicated than the process for a conventional tokamak for the following reasons:

1. The center-post is cooled by water. This places severe design constraints on design options with lithium as coolant and/or breeder. Lithium has the best potential for a high temperature system and has the capability of handling high neutron wall loading.

2. To reduce the capital cost, it will be attractive for a fusion power plant to operate with a high neutron wall loading (> 5 MW/m^2). Solid breeder blanket concepts have limited potential to handle neutron wall loading greater than 3 MW/m^2.

3. For a low-aspect-ratio tokamak design, the recirculating power can be high, due to the current-drive power and the high Joule losses in the normal coil system, including the center-post. Therefore, an efficient power conversion system is needed. This recirculation power can be much higher than a conventional tokamak.

With limited resource available for the low-aspect-ratio tokamak assessment, an attractive blanket for the low-aspect-ratio tokamak design that can satisfy both performance and safety requirements has not been identified. Table 8.3-VIII lists all the

Table 8.3-VIII.
Assessment of Blanket Options for a Low-Aspect-Ratio Tokamak Power Plant[a]

Blanket concept						
Structure	SiC Composite	V-alloy	V-alloy	Ferritic steel	Ferritic steel	Ferritic steel
Coolant	He	Li	He	LiPb	He	H_2O
Breeder	Li_2O	Li	Li	LiPb	Li_2O	LiPb
Blanket pressure	5–20 MPa	few atm	5-20 MPa	few MPa	5–20 MPa	20 MPa
Thermal Efficiency[b]	49%	46%	**33%**	**33%**	46%	**33%**
Neutron wall loading capacity						
at 3 MW/m^2	OK	OK	OK	OK	OK	OK
at 6 MW/m^2	**No**	OK	OK	**No**	**No**	OK
Safety concerns	–	**Li/water**	**Li/water**	–	–	–

[a] Issues specific to low-aspect-ratio tokamak designs with water-cooled center-posts are listed. Each blanket concept also has "generic" critical issues (see text).

[b] The thermal efficiency is the net thermal efficiency of the power cycle.

blanket options considered, each with some critical issues specific to low-aspect-ratio tokamak tokamak power plants. It should be noted that each blanket concept has some "generic" critical issues independent of the plasma operating mode: (1) development of low-activation structural material (noting small data base for SiC composites and DBTT issues for ferritic steels); (2) considerably higher afterheat in designs with ferritic steels; (3) Polonium production in designs with LiPb as coolant or breeder (a waste-disposal issue); (4) tritium contamination and clean-up of the coolant in water-cooled design; and (5) MHD pressure drop in lithium self-cooled designs (may require insulating coating).

It appears that the only blanket concepts which can avoid the safety concerns over the water-lithium combination will have modest thermal performance and wall loading limits, and will employ ferritic steel as the structural material. There are critical issues yet to be resolved for these blankets, such as the low irradiation temperature of the structural material which could cause DBTT issues and the modest cycle thermal efficiency (33%). If the recirculation power in the low-aspect-ratio tokamak design remains high, then the net thermal efficiency will be very low.

While we could not identify a high-performance blanket for the low-aspect-ratio tokamak power plant, in order assess the potential advantage of this concept, it is decided to use a high-performance blanket (Li/V blanket of ARIES-II) as the reference blanket and to determine how attractive the low-aspect-ratio tokamak concept can be. It is clear that this blanket would not be compatible to the water-cooled center-post, due to the potential lithium-water reaction.

8.3.6.2. Thermal efficiency

The large recirculating power for the low-aspect-ratio tokamak design reduces the net efficiency of the power plant. The effect of the lower thermal efficiency is reflected by the higher COE from the system evaluation. In addition, a low net efficiency has some other effects which are not assessed by the system evaluation. One of the possible impact is the thermal pollution which is caused by the large amount of rejected waste heat. Also, the large thermal power outlet will limit the possible choice of site selection. For the Starlite design goal, a net efficiency of $\sim$40% was selected.

Since we could not identify a high-performance blanket for the low-aspect-ratio tokamak power plant, we parametrically assess the impact of the net thermal efficiency of the power cycle. Figure 8.3-8 shows the net efficiency of the power plant η_{net} as a function of the recirculating power for two different net thermal cycle efficiencies. For the reference Starlite low-aspect-ratio tokamak (1000 MWe net electric output with $\sim$1,500 MW

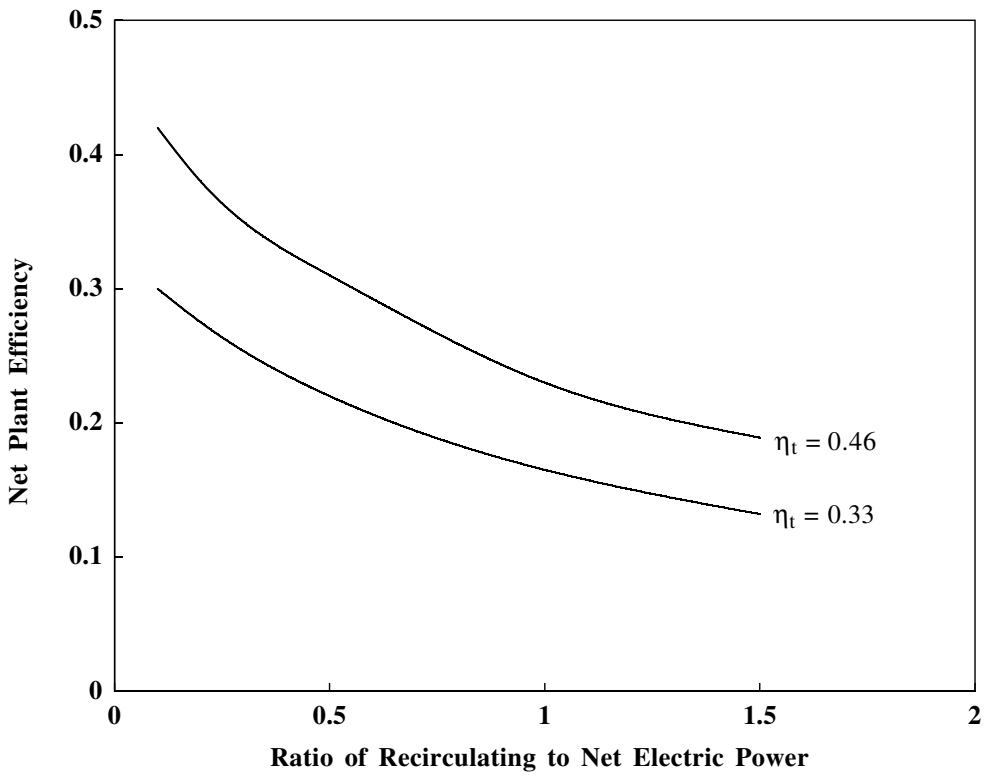

Figure 8.3-8. The net plant efficiency, η_{net} as a function of recirculating power fraction for different net thermal cycle efficiencies. The Starlite goal is a net plant efficiency of $\sim$40%.

recirculating power) which "assumes" a high-performance blanket ($\eta_{th} = 46\%$), the net plant efficiency is very low (17%). If the net thermal efficiency of the system is only 33%, the net plant efficiency will be lower than 13%!

This example clearly indicates that: (1) it is essential to reduce the recirculating power in the low-aspect-ratio tokamak to $\lesssim$500 MWe, and (2) it is essential to use a high-performance blanket option, *i.e.,* the most important parameter for the selection of the low-aspect-ratio tokamak blanket is the thermal conversion efficiency because of the potentially high recirculating power. It should be noted that blanket designs which are consistent with the low-aspect-ratio tokamak requirement tends to have low net thermal efficiency. More efficient blanket systems probably are not compatible with the low-aspect-ratio tokamak design, either with higher wall loading, or with a water-cooled center-post.

8.3.7. Divertor Assessment

Power and particle handling are two of the most difficult design problems for magnetic confinement devices. The high peak surface heat flux and target plate erosion rate are primary concerns of the divertor design, followed by the control of impurities migration and helium ash removal. During the normal operation of a fusion power plant, the goal of peak surface heat flux at the divertor plate of $\sim$5 MW/m^2 has been selected for robustness of the engineering design, while maintaining a reasonably high coolant outlet temperature for efficient thermal power conversion. Presently, the divertor design approach is to find options for distributing the plasma transport power to a large enough surface area in order to reduce the peak surface heat flux to meet the engineering goal.

For comparison, the peak surface heat flux at the outboard divertor plate for the Starlite low-aspect-ratio reference was estimated and compared with the single null ITER-EDA [35] and Starlite reversed-shear reference design. It is assumed that the transport power from the plasma core is transferred to the inboard and outboard scrape-off-layers, and then to the collector plates at the divertor by following the separatrix geometry. A relatively deep outboard slot ($\sim$1 m) is also assumed to help the trapping of neutrals and reduce electron temperature and sputtering at the target plate by allowing radial transport into the private flux region below the $\times$-point. The device geometry and transport power parameters are given in Table 8.3-IX.

The peak heat flux depends on the power balance leading to the power deposited at the scrape-off-layer (P_{SOL}), the magnetic flux expansion between the plasma mid-plane and divertor target, and the width of the scrape-off layer, and is given by:

$$Q_{peak} \;=\; \frac{0.7\,P_{SOL}}{2\pi R_s \lambda_d}\,, \tag{8.3-10}$$

where R_s is the major radius at the strike point, λ_d the width of the heat flux profile on the target, (taking into the inclination of the target plate), and the factor of 0.7 represents the power distribution between the regions outside and inside of the separatrix. In these estimates, we have accounted for the expected Bremsstrahlung and line-radiation losses in the core, up/down and in/out distributions of inboard and outboard scrape-off layer power flow that is consistent with the experimental database from ASDEX, PDX and DIII-D double-null operation [36]. The in/out power balance for the ITER single-null design is consistent with the single-null ELMing H-mode results from DIII-D [37].

Respective peak heat flux estimates are presented in Table 8.3-IX. Based on Table 8.3-IX, it is obvious that a higher peak heat flux reduction is necessary for the

Table 8.3-IX.
Simple Estimate of Peak Divertor Heat Fluxes

		Starlite Reference	
	ITER-EDA	Reversed-shear	Low-A
Major radius (m)	8.14	5.12	4.4
Aspect ratio	2.9	4	1.25
Configuration	single-null	double-null	double-null
Fusion power (MW)	1,500	1,881	3,952
α-particle power (MW)	300	376	790
Current-drive power (MW)	100	67	458
Transport power (MW)	400	443	1,248
Core radiation fraction	0.40	0.35	0.35
Up and down split	NA	1:1	1:1
Outboard and inboard split	1.3:1	4:1	4:1
Lower/outboard P_{SOL} (MW)	134	125	354
Divertor radiation fraction	0.3	0.3	0.3
Mid-plane λ_{mp} (cm)$^{(a)}$	1	1	1/2
SOL flux expansion	4	4	4
Target plate angle (°C)	20	20	20
Divertor λ_d (cm)$^{(a)}$	11.7	11.7	11.7/23.4
R_s (m)	8	4.7	4.4
Q_{peak} (MW/m^2)	17	18.4	53/26.5

$(a)\lambda$ denotes the radial energy e-folding length.

low-aspect-ratio tokamak design even assuming that certain processese may increase the mid-plane scrape-off layer thickness to 2 cm [38]. Enhanced radiation by seeding the edge-plasma by impurities (*e.g.,* Ne, Ar, Fe, Kr) and the addition of neutral gas puffing (*e.g.,* D_2) in the divertor have been shown to be effective in reducing the peak divertor heat flux and target plate plasma temperature by increasing the divertor density and radiation losses. These can possibly be utilized to reach the design goal of peak heat flux of $\sim$5 MW/m^2 for the ITER design. We would expect similar technique can also be applied to the Starlite designs.

8.4. SYSTEMS ASSESSMENT

The low-aspect-ratio (LAR) tokamak is not as developed theoretically nor experimentally as the other tokamak regimes discussed in this report. The role of systems analysis for the LAR tokamak, therefore, is to identify high-leverage parameters affecting power-plant design, rather then to suggest specific values for these parameters that minimize the cost-of-electricity (COE). The design parameters examined in this analysis are: the plasma minor radius, a_p; the factor f_{TF} by which the toroidal dimension of the cross section of the outer log of the toroidal-field (TF) leg is increased; the plasma ion temperature, T_i; the inboard shield thickness, $\delta_{S,I}$; the factor f_Ω by which the ohmic dissipation in the center-post is reduced due to shaping of the center-post; and the plasma toroidal β. An additional parameter relevant to the center-post shaping is the factor f_V by which the center-post volume is increased due to shaping. The plasma aspect ratio, A, is also an important design parameter, but resource limitations only permitted parametric system examination of designs at $A = 1.25$, suggested in Ref. [39]. Nominal values for the above variables are listed in Table 8.4-I.

8.4.1. Low-Aspect-Ratio-Tokamak Systems Models

Most of the models used in the ARIES Systems Code (ASC) for the low-aspect-ratio tokamak are described in Ref. [17, 40]. Those models that are specific to the low-aspect-ratio tokamaks (*e.g.*, a scaling for current-drive efficiency, γ_B) are discussed as needed in the text. The plasma equilibrium (*e.g.*, magnetic topology, β, *etc.*), current-drive, and other physics results are based upon the analyses of the STREAC19 equilibrium presented in Sec. 8.2. All analysis is done for a 1-GWe, commercial power plant with a vanadium blanket and shield design that is a refinement of the ARIES-II blanket and shield design and is described in Sec. 6. Modifications to the blanket and shield design

Table 8.4-I.
Nominal Values used in Parametric Analysis

Plasma aspect ratio	1.25
Equilibrium	STREAC19$^{(a)}$
Plasma β	36.3%
Plasma minor radius (m)	4.0
Center-Post dissipation scale factor, f_Ω	0.61
Center-Post volume scale factor, f_V	2.03
TF-Coil cross-sectional scale factor, f_{TF}	5.0
Plasma ion temperature (keV)	12.0
Inboard shield thickness, $\delta_{S,I}$ (m)	0.3
Net electrical power (GWe)	1.0

(a)See Sec. 8.2.

specific to LAR are described in Sec. 8.3. These modifications include the elimination of the inboard blanket and a reduction in the thickness of the inboard shield to 0.3 m (the minimum thickness that ensures Class-C waste-disposal rating for the center-post after its approximately two-full-power-year lifetime). The poloidal-field (PF) coils are superconducting coils; whereas the TF coils are normal conducting coils. A Level of Safety Assurance (LSA) rating of LSA=2 has been assumed without regard for possible incompatibility of blanket and center-post coolants, and appropriate cost credits have been taken. All costs are reported in 1992 dollars.

The base configuration of the LAR fusion power core (FPC) is shown in Fig. 8.4-1. The inboard first wall conforms to a flux surface and serves as a limiter to the plasma surface inboard of the null. Vertical space is provided above the null for a divertor chamber that captures the plasma exhaust from the outboard plasma surface. The center-post cross section expands above the equatorial plane as allowed by the first wall and inboard shield to provide maximum shaping of the center-post conductor in order to reduce Joule losses.

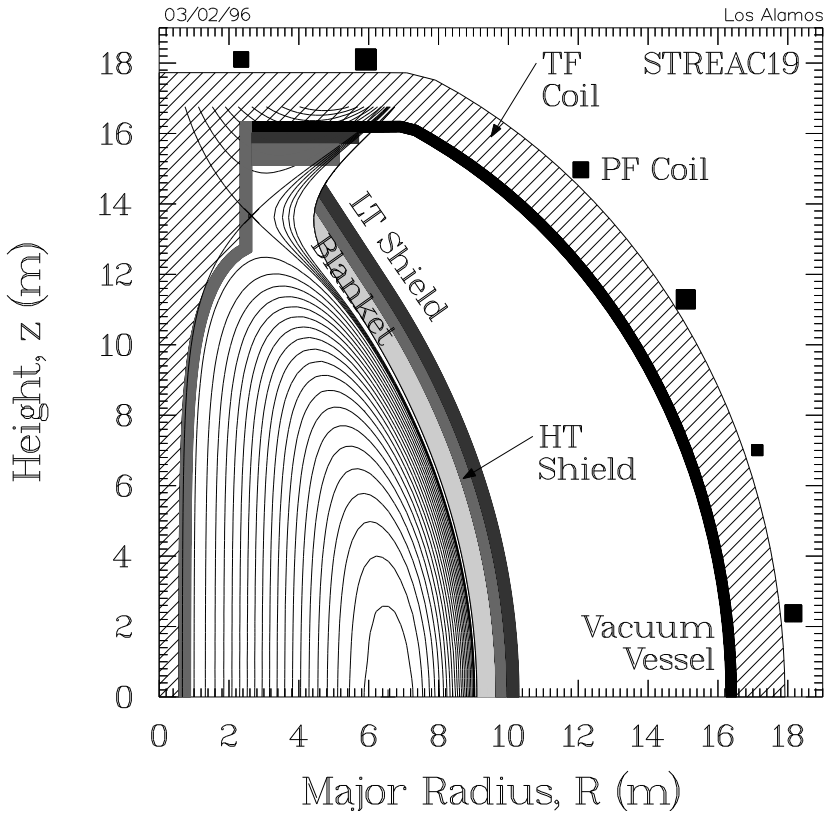

Figure 8.4-1. Elevation view of an upper-half quadrant of the LAR fusion power core.

8.4.2. Sensitivity Studies

8.4.2.1. Plasma minor radius

The most basic design parameter is the physical size of the tokamak. Typically, the ASC determines the plasma minor radius that minimizes the cost of electricity (COE) for a specified plasma aspect ratio and ion temperature with an internal scan of minor radius. The COE for such a scan in a_p is shown in Fig. 8.4-2 for the LAR design. The COE for the LAR generally displays a minimum in minor radius resulting from the tradeoff of maximizing the Fusion Power Core (FPC) mass power density (MPD) and of maximizing the engineering gain ($1/\epsilon$, where ϵ is the recirculating power fraction), as is shown in Fig. 8.4-3. Decreasing the plasma minor radius decreases the blanket, shield, and coil masses and increases the MPD. For an LAR-based power plant, the center-post dissipation dominates the recirculating-power losses that determine the engineering gain. Decreasing the plasma minor radius increases the ohmic dissipation in the resistive TF

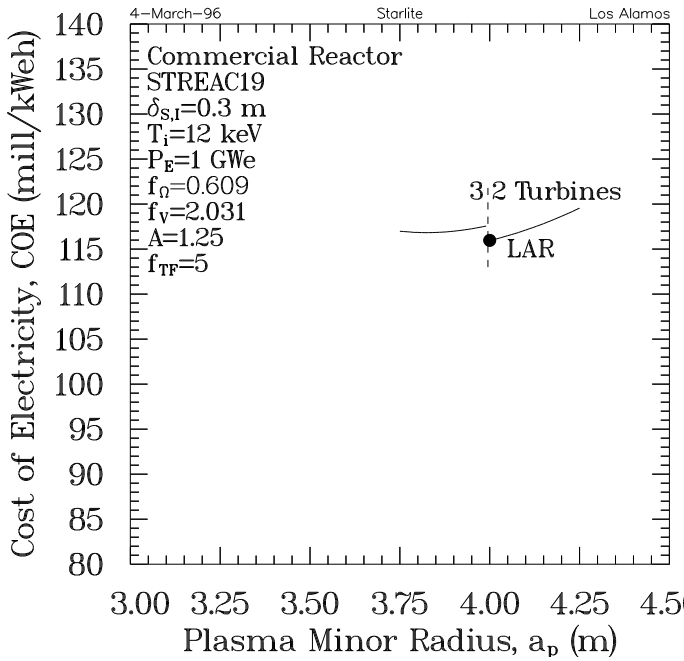

Figure 8.4-2. Cost of electricity as a function of plasma minor radius calculated internally to the ASC for the given LAR parameters.

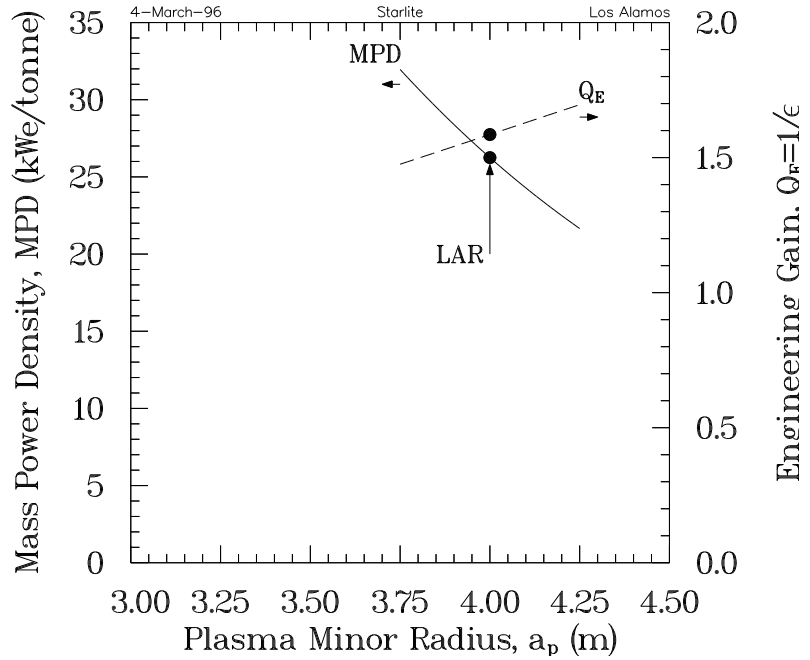

Figure 8.4-3. The mass power density (left scale) and the engineering gain (right scale) for the minor-radius variation of Fig. 8.4-2.

coils, because the center-post cross-sectional area decreases with decreasing plasma minor radius, and the center-post resistance and ohmic dissipation then increase.

The minimum of COE in Fig. 8.4-2 is also affected by the discrete nature of turbine capacity. The ASC costing algorithms limit the capacity of a single turbine to 1,360 MWe which gives rise to the discontinuity in the COE *versus* minor radius shown in Fig. 8.4-2. Because the ASC models for the LAR project large (1,185 MW) center-post dissipations, the gross electric power is always near the transition point where the number of turbines required changes from two to three. Minor changes in the assumed parameters listed in Fig. 8.4-2 can move the location of this transition point to larger plasma minor radius and eventually cause the minor radius that minimizes the COE to jump in a discontinuous fashion to a local minimum where $\partial \mathrm{COE}/\partial \mathrm{a_p} = 0$, as opposed to the extremum shown in Fig. 8.4-2. Although this jumping effect does not significantly affect the COE, discontinuities in various variables displayed in subsequent parametric curves are possible.

8.4.2.2. Size of the outboard TF-coil cross section

Because the LAR tokamak has a large recirculating power fraction, methods to reduce the recirculating power should be exercised. One such method is to increase the cross sectional area of the outboard TF-coil leg. In the ASC the "base" cross section of the outboard TF-coil leg is a rectangle with a toroidal dimension which is equal to the length of one side of the 16-sided polyhedronal cross section of the center-post in the equatorial plane. The radial leg of this "base" cross section is always assumed to be increased by a factor $f_r = 2.5$. In order to ass the impact of the change in the size of the outboard TF-coil cross section, the toroidal leg of this "base" cross section is increased by a variable factor f_{TF}. The cost-of-electricity sensitivity to f_{TF} is shown in Fig. 8.4-4. The minimum in the COE with f_{TF} represents the classic tradeoff between maximizing mass power density and maximizing the engineering gain, as is shown in Fig. 8.4-5. The engineering gain increases with increasing f_{TF}, because increasing f_{TF} increases the cross sectional area for the outboard TF coil that, in turn, decreases the coil resistance (resistance = resistivity $\times$ conductor length / conductor area) and the power dissipated in the outboard TF-coil leg. Increasing f_{TF} also increases the mass of the outboard TF-coil leg, thus decreasing the mass power density.

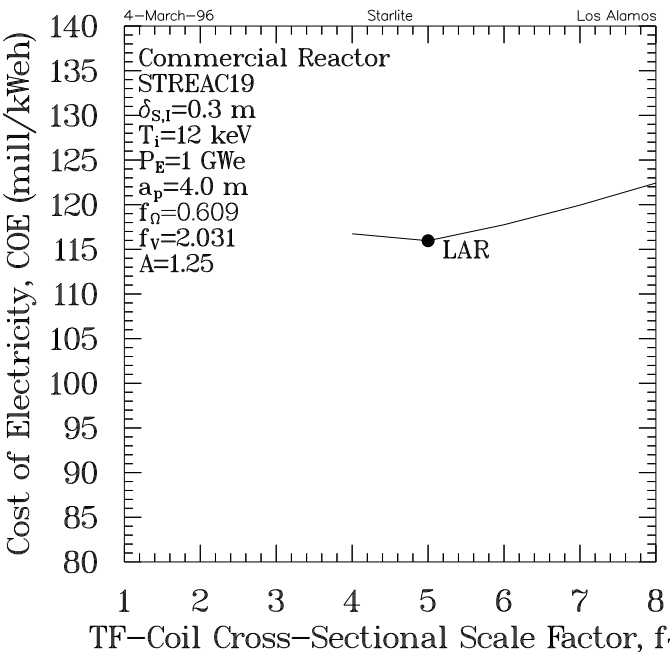

Figure 8.4-4. The cost of electricity for LAR parameters as a function of the outboard TF-coil cross-sectional scale factor.

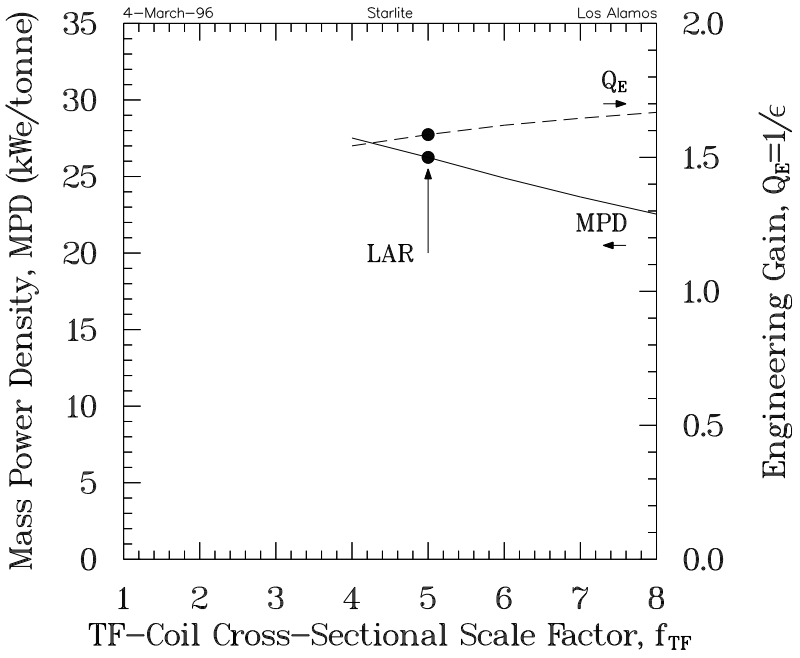

Figure 8.4-5. The mass power density (left scale) and the engineering gain (right scale) for the minor-radius variation of Fig. 8.4-4.

8.4.2.3. Plasma ion temperature

The cost-of-electricity sensitivity to variations in the plasma ion temperature is shown in Fig. 8.4-6. The temperature that minimizes the COE also maximizes the mass power density, as is shown in Fig. 8.4-7. The engineering gain does not play a role in the optimization of the plasma ion temperature, because the only component of the engineering gain that is plasma-temperature dependent is the current-drive efficiency, and the current-drive power is negligible ($\lesssim$7 MW) for this equilibrium (Sec. 8.2.3). At low temperatures (*i.e.*, $\leq$12 keV), the mass power density increases slightly with increasing temperature because $\langle\sigma v\rangle/T_i^2$ is increasing with increasing temperature until its maximum at $\approx$15 keV. The MPD decreases with increasing temperature above the optimum temperature because of decreased reactivity (*i.e.*, $n^2\langle\sigma v\rangle$). However, the plasma density decreases (at constant β) and the fusion products are thermalized more slowly which increases the hot alpha-particle pressure and decreases the fuel pressure (see Fig. 8.4-7), and requires a higher toroidal-field strength, which increases TF-coil costs for the same net electrical power.

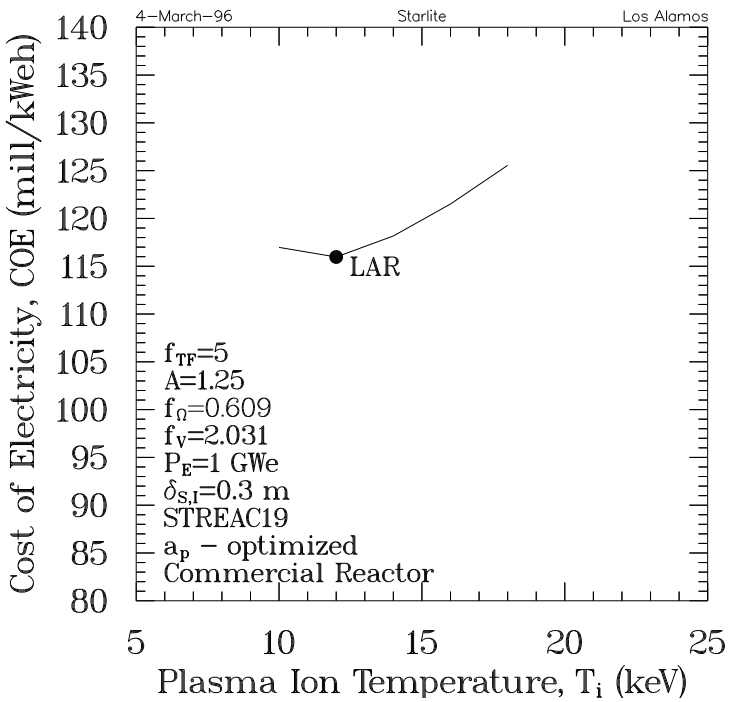

Figure 8.4-6. The cost of electricity for LAR parameters as a function of the plasma ion temperature. Each point along the curve represents the COE optimum in plasma minor radius, a_p.

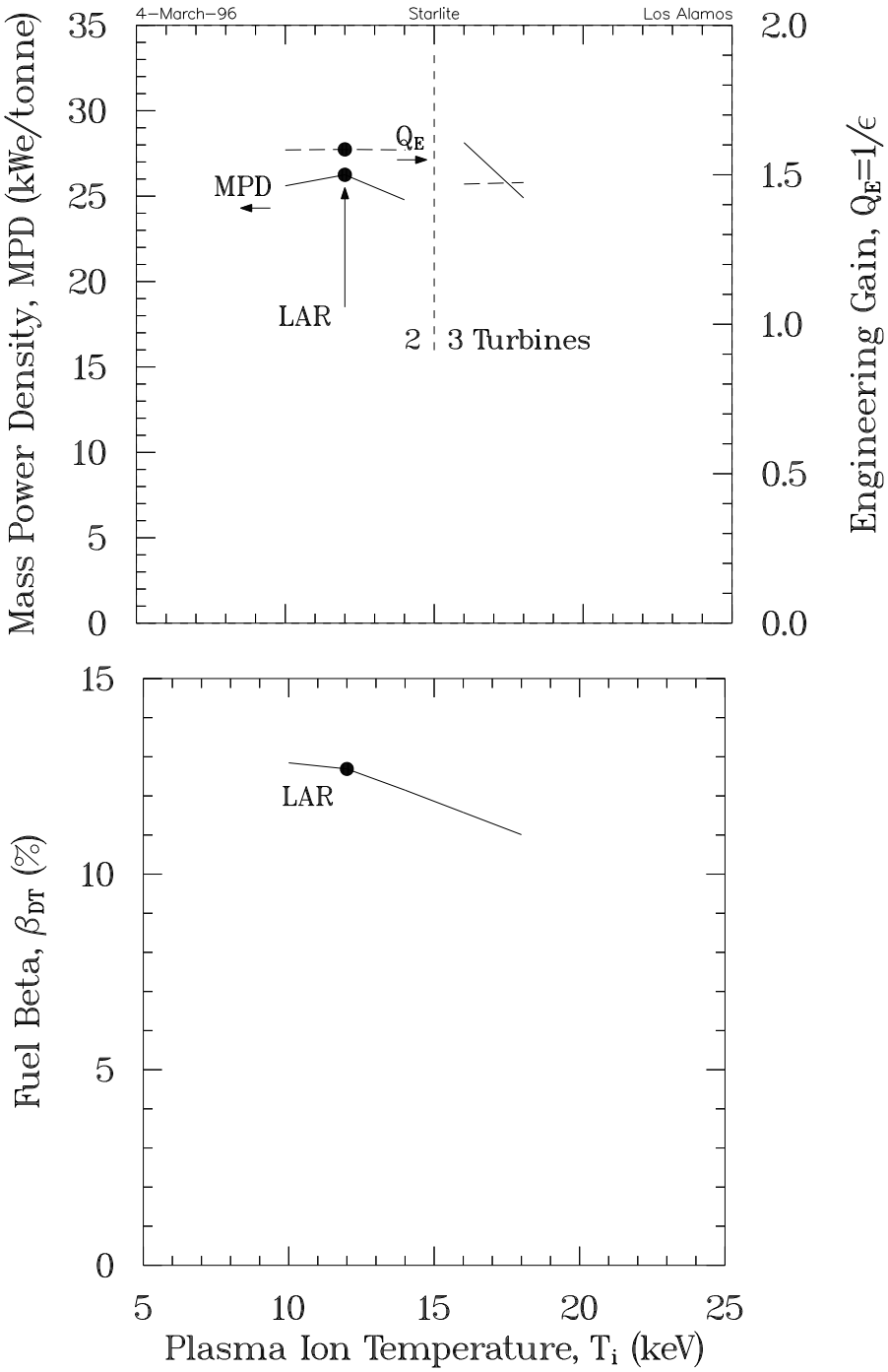

Figure 8.4-7. Variation of the mass power density (left scale, top frame) and engineering gain (right scale, top frame) and the fuel β (bottom frame) for the ion-temperature variation of Fig. 8.4-6.

As mentioned above, current drive does not play a role in the determination of the optimum temperature, because the STREAC19 equilibrium maximizes the bootstrap-current fraction at a value of $f_{BC} = 0.997$. Attaining a bootstrap-current fraction approaching unity is essential for a low-aspect-ratio tokamak power plant because even at a high bootstrap-current fraction of $f_{BC} = 0.9$, the current-drive power (including system efficiency) exceeds 600 MWe.

8.4.2.4. Inboard shield thickness

The impact of an 0.3-m thick inboard shield surrounding the center-post is indicated in Table 8.4-II. The first column of Table 8.4-II represent the "base" case with an 0.3-m thick inboard shield. For Case A, the inboard shield has been removed. Without an inboard shield the space that would have been allocated for shielding can be used as additional center-post conductor to reduce the center-post dissipation and associated recirculating power and to increase the engineering gain. Because the engineering gain is raised for all plasma minor radii, the COE minimizes at a lower plasma minor radius,

Table 8.4-II.
Effect of Removing the Inboard Shield[(a)]

Case	Base	A	B	C
Inboard shield thickness (m)	0.30	0.	0.	0.
Plant capacity factor	0.76	0.76	0.76	0.59
First-Wall fluence lifetime (MWy/m^2)	12.0	12.0	12.0	12.0
Center-Post fluence lifetime (MWy/m^2)	12.0	12.0	0.3	0.3
Plasma minor radius (m)	4.00	2.40	2.55	2.46
Engineering gain Q_E	1.58	1.83	1.92	1.87
Mass power density (kWe/tonne)	26.2	53.9	47.1	55.6
Cost of electricity (mill/kWeh)	116.0	88.7	163.5	182.0

(a) For the fixed parameters of Table 8.4-I.

thus increasing the mass power density. The COE is 20 mill/kWeh lower for Case A relative to the "base" case with an inboard shield. However, this second case does not account for the consequences of not having an inboard shield, and the conter-post does not qualify for Class-C low level waste.

The fluence lifetime of the center-post should be reduced to 0.3 MWy/m^2 to meet the requirements for Class C waste disposal (Sec. 8.3), affecting just the replacement cost for the center-post (Case B of Table 8.4-II). No penalty has been assessed for an expected 3% increase in the center-post resistivity. For this case the optimum COE occurs at a larger plasma minor radius than for Case A because the center-post replacement cost has risen relative to the cost associated with recirculating power. The COE of Case B is 48 mill/kWeh higher than for the base case.

Lastly, the plant availability is reduced from 0.76 to 0.59, to simulate a center-post lifetime of ≈1.44 months and a replacement time of ≈ 1 month (Case C of Table 8.4-II). Although the cost of electricity is explicitly dependent upon $1/p_f$, the economics governing the optimization is also influenced by the plant availability factor. Reducing the plant factor places a greater emphasis on reducing production costs (*i.e.*, mass power density and associated costs). This case is 66 mill/kWeh higher than for the base case.

It should be noted that for the four cases of Table 8.4-II, the current-drive power is negligible (*i.e.*, ∼10 MW). If a more careful analysis of MHD equilibrium and stability, current drive, and profile control indicates the current-drive power is not effectively zero, then eliminating the inboard shield does not have nearly as significant an effect on the COE as is indicated herein, because of the added cost of current drive.

8.4.2.5. Center-post shaping

For the purposes of analyzing the effect of shaping the center-post, the unshaped center-post is characterized by: (1) a conductor filling fraction $\lambda = 0.7$, (2) a Cu resistivity $\eta = 2 \times 10^{-8}$ ohm-m, (3) a height H_{CP} and a radius R_{CP}, (4) a current density $j_{CP} = I_{CP}/\pi R_{CP}^2$, (5) a volume $V_{CP} = \pi R_{CP}^2 \lambda H_{CP}$, and (6) a ohmic dissipation $P_{CP} = \eta I_{CP} j_{CP} H_{CP}/\lambda$. The volume of the shaped center-post can be expressed as $V_{CP}^s = V_{CP} f_V$, where

$$f_V = \left[\pi \int_0^{H_{CP}} R^2 dz - (1-\lambda) V_{CP}\right] / \lambda V_{CP} \,. \tag{8.4-1}$$

Similarly, the ohmic dissipation in the shaped center-post can be expressed as $P^s_{CP} = P_{CP} f_\Omega$, where

$$f_\Omega = \frac{\lambda R^2_{CP}}{H_{CP}} \int_0^{H_{CP}} \frac{dz}{R^2 - (1-\lambda) R^2_{CP}} \,. \tag{8.4-2}$$

The effect of shaping the center-post on the COE is indicated in Table 8.4-III for the LAR parameters. A significant savings of 25 mill/kWeh is obtained by shaping the center-post, suggesting that all LAR-tokamak power-plant designs should invoke center-post shaping. This reduction in COE is possible because the additional center-post conductor reduces the center-post dissipation and the recirculating power by 469 and 435 MW, respectively. The reduced recirculating power permits a reduction in machine size (*i.e.*, a_p) to increase MPD and further decrease COE.

Table 8.4-III.
Effect of Shaping the Center-Post[(a)]

	With shaping	Without shaping
Center-Post dissipation scale factor, f_Ω	0.609	1.0
Center-Post volume scale factor, f_V	2.031	1.0
Center-Post dissipation (MW)	1,185	1,654
Gross electrical power (GWe)	2,708	3,143
Plasma minor radius (m)	4.00	4.50
Engineering gain	1.58	1.47
Mass power density (kWe/tonne)	26.2	21.7
Cost of electricity (mill/kWeh)	116.0	139.0

(*a*) For the fixed parameters of Table 8.4-I.

8.4.2.6. Plasma β

The LAR tokamak offers high beta, but also carries along the disadvantages of high recirculating power that have been evident in the previous parametric variations. One question that arises immediately for the LAR tokamak is how high must the plasma β be to suppress the deleterious effects of the recirculating power? The variation in the COE with plasma β is shown in Fig. 8.4-8 for LAR parameters. Note that this variation is not based on self-consistent plasma equilibria. Rather the achievable β of the base equilibrium (36%) is arbitrarily increased.

The benefits of increasing the β are a reduction in plasma size (*i.e.*, a_p) and an increase in mass power density, while simultaneously increasing the engineering gain. The Starlite requirement and goal for the COE are 65 and 80 mill/kWeh, respectively, as indicated in Sec. 3 and Ref. [1]. Extrapolation of the results of Fig. 8.4-8 indicate that $\beta \approx 100\%$ is required just to meet the Starlite COE requirement with the current-drive power effectively set to zero.

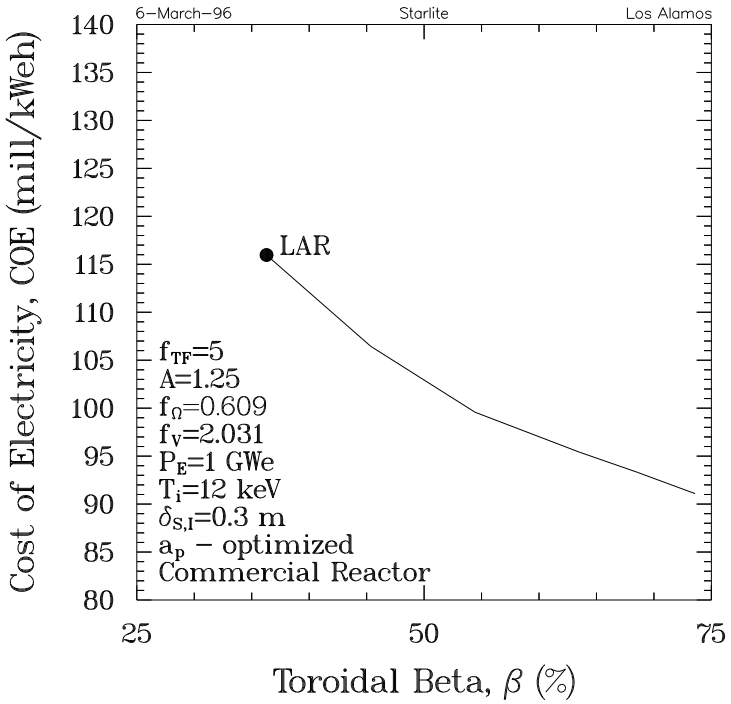

Figure 8.4-8. The cost of electricity for LAR parameters as a function of the plasma β. Note that this variation is not based on self-consistent plasma equilibria. Rather the achievable β of the base equilibrium (36%) is arbitrarily increased.

8.4.3. Design Point Determination

Although the LAR tokamak analysis is not as complete nor as self-consistent as the analysis of the other tokamaks in this report, a list of parameters for the reference design used in the systems analysis are given in Tables 8.4-IV through 8.4-VI.

Table 8.4-IV.
Low-Aspect-Ratio (LAR) Power-Plant Physics Parameters

Plasma major toroidal radius, R_T (m)	5.00
Plasma minor radius, a_p (m)	4.00
Plasma vertical elongation, $\kappa_\times$	3.00
Plasma vertical elongation, κ_{95}	3.40
Plasma triangularity, $\delta_\times$	0.45
Plasma triangularity, δ_{95}	0.55
Plasma aspect ratio, $A = R_T/a_p$	1.25
On-axis safety factor, q_0	2.94
Circularized safety factor, q_*	3.54
Plasma-edge safety factor, q	28.87
Troyon coefficient, C_T (Tm/MA)	0.06
Plasma β	0.36
Plasma poloidal β	1.42
Stability parameter, $\epsilon\beta_p$	1.13
Peak-to-average density, n_0/n	1.57
Peak-to-average temperature, T_0/T	1.06
Normalized edge density, n_E/n	0.29
Ion temperature, T_i (keV)	12.00
Electron temperature, T_e (keV)	12.19
Ion density, n_i (10^{20} m^{-3})	1.00
Electron density, n_e (10^{20} m^{-3})	1.24
Particle-to-energy confinement time ratio, τ_p/τ_E	4.00
Ion-to-electron energy confinement time ratio, τ_{Ei}/τ_{Ee}	1.00
Lawson parameter, $n_i\tau_E$ (10^{20} m^{-3}s)	4.89
ITER-89P scaling [41] multiplier, H_{89P}	3.02
On-axis toroidal field, $B_{\phi 0}$ (T)	1.77
Radiation fraction, f_{RAD}	0.32
Plasma current, I_p (MA)	40.06
Bootstrap-current fraction, f_{BC}	1.00
Current-drive power to plasma, P_{CD} (MW)	7.27
Current-drive efficiencies:	
I_{EX}/P_{CD} (mA/W)	16.52
γ (10^{20} A/W-m^2)	34.23

Table 8.4-V.
Low-Aspect-Ratio (LAR) Power-Plant Engineering Parameters

Field at TF coil, $B_{\phi c}$ (T)	15.95
Center-post resistive losses (MW)	1,185
Total TF resistive losses (MW)	1,565
TF-coil current density, j_{TF} (MA/m^2)	27.49
Magnetic-field energy, W_B (GJ)	25.24
Total specific energy, W_B/M_c (MJ/tonne)	2.63
Fusion power, P_F (GW)	4.53
Neutron power, P_N (GW)	3.62
Average neutron wall loading, I_w (MW/m^2)	2.23
Peak neutron wall loading, $\hat{I}_w$ (MW/m^2)	3.14
Neutron fluence life, $I_w\tau$ (MWy/m^2)	12.00
Average blanket energy multiplication	1.37
Average first-wall heat flux, q_w (MW/m^2)	0.27
Blanket power density, P_{TH}/V_{BLK} (MW/m^3)	13.87
Current-drive system efficiency, η_{CD}	0.95
Thermal conversion efficiency, η_{TH}	0.46
Thermal power (GWth):	
peak, $\hat{P}_{TH}$	5.89
average, P_{TH}	5.89
Auxiliary site power, P_{AUX} (MW)	108.33
Primary loop pumping power (MW)	27.08
Gross electrical power, P_{ET} (GWe)	2.71
Net electrical power, P_E (GWe)	1.00
Recirculating-power fraction, $\epsilon = 1/Q_E$	0.63
Plasma gain, $Q_p = P_F/P_{CD}$	622.66
Engineering gain, Q_E	1.59
Net plant efficiency, $\eta_p = \eta_{TH}(1-\epsilon)$	0.17
Plant capacity factor, p_f	0.76
Masses (tonne):	
First wall	17
Blanket and reflector	259
Shield	8,036
TF coils	8,167
PF coils	1,447
Fusion power core	2,4863
Mass power density, MPD (kWe/tonne)	26.25
Level of Safety Assurance, LSA	2

Table 8.4-VI.
Low-Aspect-Ratio (LAR) Power-Plant Economic Parameters (1992 $)

Acct. No.	Account Title	Million Dollars
20.	Land and land rights	10.4
21.	Structures and site facilities	433.5
22.	Reactor plant equipment	2,209.9
22.1.1	First wall, Blanket, and Reflector	78.7
22.1.2	Shield	356.2
22.1.3	Magnets	619.7
22.1.3.1	TF coils	507.4
22.1.3.3	PF coils	112.4
22.1.4	Supplemental heating systems	127.6
22.1.5	Primary structure and support	109.6
22.1.6	Reactor vacuum systems	140.9
22.1.7	Power supplies	137.3
22.1.8	Impurity control	16.7
22.1.9	Direct energy conversion system	0.0
22.1.10	ECRH breakdown system	4.3
22.1	Reactor equipment	1,591.0
22.2	Main Heat Transfer and Transport	365.8
23.	Turbine plant equipment	628.4
24.	Electric plant equipment	164.5
25.	Miscellaneous plant equipment	90.6
26.	Special materials	27.0
90.	Total direct cost	3,564.4
91.	Construction services and equipment	427.7
92.	Home office engineering and services	185.3
93.	Field office engineering and services	213.9
94.	Owner's costs	658.7
96.	Project contingency	852.2
97.	Interest during construction (IDC)	975.1
98.	Escalation during construction (EDC)	0.
99.	Total capital cost	6,877.3
		Constant dollars
[90]	Unit direct cost, UDC ($/kWe)	3,564.4
[94]	Unit base cost, UBC ($/kWe)	5,902.2
[99]	Unit total cost, UTC ($/kWe)	6,877.3
	Capital return (mill/kWeh)	99.86
[40-47,51]	O&M (1.4%) (mill/kWeh)	9.16
[50]	Blanket replacement (mill/kWeh)	6.38
	Decommissioning (mill/kWeh)	0.50
[02]	Fuel (mill/kWeh)	0.07
	Cost of electricity, COE (mill/kWeh)	115.97

8.5. SUMMARY & CONCLUSIONS

The assessment of low-aspect-ratio tokamak power plants included detailed physics calculations, system studies, and preliminary engineering design considerations. The physics analyses yielded equilibria that are stable to all MHD modes (with a wall present) and require very little current drive power ($\lesssim$10 MW) due to bootstrap fractions approaching unity. These equilibria had the following characteristics: aspect ratio of 1.25, elongations of 3 and β as high as 40%. It is noted that these cases would require a vertical feedback control system and a conducting wall to stabilize the external kink mode. The sensitivity of the current drive power requirements to variations in plasma profiles is an important issue and must be addressed in future studies.

Using the cases noted above, system studies and engineering analyses were conducted. It appears that even for these cases with low current-drive power requirements, there still was significant recirculating power (*i.e.,* recirculating power fraction $\sim$0.6) associated with the resistive losses in the copper center post and return legs of the toroidal field coils. In this context, minimizing the amount of inboard shielding for the low-aspect-ratio tokamak is well known to be important for the power efficiency of the concept. However, an unshielded copper center post leads to activation levels which exceed the NRC Class-C waste-disposal limit, unless change-out times of the order of weeks are employed. Such short change-out times lead to unacceptable costs of electricity. Our systems and engineering analyses indicated that it is desirable to add about 30 cm of shielding to the center post. This level of shielding helps significantly to reduce the waste disposal problem and the associated deleterious effect on cost of electricity. At the same time, however, the addition of this shielding increases the resistive losses in the center post, however, the net effect is beneficial with respect to the unshielded case.

In addition to concerns about the design of the center post, preliminary engineering evaluations also identified constraints with regard to the blanket and divertor. In the context of blanket design, the use of water in the center-post makes the use of liquid lithium in the blanket problematic due to safety issues. Additional barriers to leakage would be necessary and substantial additional analysis would have to be performed to satisfy licensing and regulatory requirements if liquid lithium were to be used in the blanket. The impact of ruling out liquid lithium in the blanket is to reduce the bulk heat removal capabilities of the concept and, thus, further reduce the overall plant efficiency which is already low ($\sim$17%). Finally, the divertor problem appears especially severe for the low-aspect-ratio tokamak concept because the divertor surface area available at low major radius is so restricted.

REFERENCES

[1] L. M. Waganer, F. Najmabadi, M. S. Tillack, and the ARIES Team, "What Must Demo Do?" *Proc. IEEE 16th Symp. on Fusion Eng.,* Champaign, IL (Oct. 1995) IEEE No. 95CH35852, IEEE, Piscataway, NJ (1995).

[2] C. G. Bathke and the ARIES Team, "A Preliminary Systems Assessment of the Starlite DEMO Candidates," Los Alamos National Laboratory Report LA-UR-95-3489, *Proc. IEEE 16th Symp. on Fusion Eng.,* Champaign, IL (Oct. 1995) IEEE No. 95CH35852, IEEE, Piscataway, NJ (1995).

[3] V. S. Mukhovatov and V. D. Shafranov, "Plasma Equilibrium in a Tokamak," *Nucl. Fusion,* **11** (1971) 605.

[4] E. Rehban, "Stability Boundaries of Tokamaks with Respect to Rigid Displacements", *Nucl. Fusion,* **15** (1975) 277.

[5] Y-K. M. Peng and D. J. Strickler, "Features of Spherical Torus Plasmas," *Nucl. Fusion,* **26** (1986) 769.

[6] S. P. Hakkaraninen, R. Betti, J. P. Freidberg, *et al.*, "Natural Elongation and Triangularity of Tokamak Equilibria," *Phys. Fluids,* **B2** (1990) 1565.

[7] M. Roberto, "Natural Elongation of Spherical Tokamaks," *Nuc. Fusion,* **32** (1992) 1666.

[8] R. M. O. Galvao, S. G. Kalmykov, M. Roberto, *et al.*, "Dependence of Natural Elongation of Low Aspect Ratio Tokamak Plasmas on Current Profile," *Comm. Plas. Phys. Control. Fusion,* **15** (1993) 219.

[9] S. G. Kalmykov, "Low-Aspect-Ratio Tokamaks: Plasma Sheath Cross Section Natural Elongation as a Function of Current Density Profile," *Soviet Plas. Phys. Rep.,* **20** (1994) 844.

[10] S. C. Jardin, N. Pomphrey, and J. DeLucia, "Dynamic Modeling of Transport and Positional Control of Tokamaks," *J. Comput. Phys.,* **66** (1986) 481.

[11] M. F. Reusch and G. H. Neilson, "Toroidally Symmetric Polynomial Multipole Solutions of the Vector Laplace Equation," *J. Comput. Phys.,* **64** (1986) 416.

[12] J. Menard, Presentation at Low-A Tokamak workshop, Oak Ridge National Laboratory, Oak Ridge, TN (July 1994).

[13] J. Menard, S. C. Jardin, S. M. Kaye, *et al.*, "Ideal MHD Stability of High Beta/High Bootstrap Fraction Equilibria in NSTX," *Bull. Am. Phys. Soc.* **40** (1995) 1655.

[14] C. E. Kessel, "Bootstrap Current in a Tokamak," *Nucl. Fusion,* **34** (1994) 1221.

[15] T. K. Mau, S. C. Chiu, R. W. Harvey, "Modelling of Fast-Wave Current Drive in Standard and Second-Stability Bootstrapped Reactor Plasmas," *Proc. EPS Topical Conf. on Radiofrequency Heating and Current Drive of Fusion Devices,* Brussels, Belgium (1992) 181.

[16] A. Bondeson and D. J. Ward, "Stabilizaton of External Modes in Tokamaks by Resistive Walls and Plasma Rotation," *Phys. Rev. Lett.* **72** (1994) 2709.

[17] F. Najmabadi, R. W. Conn, *et al.*, "The ARIES-II and -IV Second-Stability Tokamak Fusion Power Plant Study—The Final Report," UCLA report UCLA-PPG-1461 (to be published); also, F. Najmabadi, R. W. Conn, *et al.*, "Directions for Attractive Tokamak Reactors: The ARIES-II and ARIES-IV Second-Stability Designs," *Proc. 14th Int. Conf. on Plasma Phys. and Controlled Nucl. Fusion Research,* Würzburg, Germany (Oct. 1992), International Atomic Energy Agency, Vienna (1993) 295.

[18] J. B. Hicks, "Toroidal Field System for Tight Aspect Ratio Tokamak Reactors," UKAEA report AEA FUS 118 (June 1991).

[19] "GlidCop, A Material for Today, A Technology for Tomorrow," SCM Metal Products, Inc., Research Triangle Park, NC (1995).

[20] R. R. Solomon, Market Manager, GlidCop, SCM Metal Products, Inc., personal communication (Sept. 1995).

[21] *1995 ASME Boiler and Pressure Vessel Code, Section II, Part D – Materials.* Am. Soc. Mech. Eng. (1995).

[22] S. A. Fabritsiev, S. J. Zinkle, and B. N. Singh, "Evaluation of Copper Alloys for Fusion Reactor Divertor and First Wall Components," *Proc. 7th Int. Conf. Fusion Reactor Mater.*, Obninsk, Russia, (Sept. 1995), to be published in *J. Nucl. Mater.*

[23] S. A. Fabritsiev, A. S. Pokrovsky, S. J. Zinkle, and D. J. Edwards, "Low-Temperature Radiation Embrittlement of Copper Alloys," *Proc. 7th Int. Conf. Fusion Reactor Mater.*, Obninsk, Russia, (Sept. 1995), to be published in *J. Nucl. Mater.*

[24] M. C. Billone and J. E. Pawel, "Summary of Recommended Correlations for ITER-Grade Type 316L(N) for the ITER Material Properties Handbook," in "Fusion Materials Semiannual Progress Report for the Period Ending Sept. 30, 1995," U.S. Department of Energy Report DOE/ER-0313/19 (to be published).

[25] M. C. Billone, "Allowable Design Stresses and Design Safety Factors for ITER Types 316L(N) Stainles Steel," Argonne National Laboratory informal report (July 1995).

[26] *Metals Handbook, Ninth Edition, Vol. 2, Properties and Selection: Nonferrous Alloys and Pure Metals,* American Society for Metals, Metals Park, OH, pp. 275-279.

[27] R. O'Dell *et al.*, "User's Manual for ONEDANT: A Code Package for One-Dimensional, Diffusion-Accelerated, Neutral Particle Transport," Los Alamos National Laboratory report LA-9184-M (1982).

[28] "Licensing Requirements for Land Disposal of Radioactive Waste," Nuclear Regulatory Commission, 10CFR part 61, Federal Register, FR 47 (1982) 57446.

[29] S. Fetter, E. T. Cheng and F. M. Mann, "Long Term Radioactive Waste from Fusion Reactors: Part II," *Fusion Eng. Design,* **13** (1990) 239.

[30] D. L. Henderson and O. Yasar, "DKR-ICF: A Radioactivity and Dose Rate Calculation Code Package," University of Wisconsin Fusion Technology Institute report, UWFDM-714, Vol. 1 (April 1987).

[31] F. M. Mann and D. E. Lessor, "REAC*3 Nuclear Data Libraries," *Proc. of an Int. Conf. held at Forschungszentrum Jülich,* Federal Republic of Germany (13-17 May 1991).

[32] L. El-Guebaly, J. Perkins, and C. Maynard, "MARS Axial Radiation Damage and Shielding Analysis," *Nucl. Technol./Fusion*, **4/2** (1983) 1171.

[33] S. Zinkle, Oak Ridge National Laboaratory, private communication, April 1995.

[34] R. F. Mattas, "Copper Alloy Selection," Presented at *ITER Blanket Workshop,* Garching, Germany, (20-24 Feb. 1995).

[35] K. J. Dietz and P. H. Rebut, " The ITER Divertor," *Proc. IEEE 15th Symp. on Fusion Eng.,* Hyannis, MA (Oct. 1993), IEEE No. 93CH3348-0, IEEE, Piscataway, NJ (1994) 604

[36] D. Hill, Lawrence Livermore National Laboratory, private communication (Nov. 1995).

[37] A. W. Leonard *et al.*, "Power balance in DIII-D during single-null ELMing H-mode plasmas," *J. Nucl. Mater.* **220-222** (1995) 325.

[38] Y-K. M. Peng, Oak Ridge National Laboratory, private communications (Nov. 1995).

[39] Y-K. M. Peng, "Prospects and Status of Low-Aspect-Ratio Tokamaks," *Trans. Fus. Technol.* **27** 138 (April 1995).

[40] F. Najmabadi *et al.*, "The Pulsar Study– A Pulsed-Tokamak Fusion Power Plant," University of California, San Diego report UCSD-ENG-003 (1996).

[41] D. E. Post, K. Borrass, J. D. Callen, S. A. Cohen, J. G. Cordey, F. Engelmann, *et al.*, "ITER Physics," International Thermonuclear Experimental Reactor documentation series No. 21 (November 1990).